E7-10126
CR-156977

Final Report, NASA Grant NSG-5155

January 17, 1977 to March 16, 1978

VOLUME I

REMOTE SENSING APPLICATIONS TO HYDROLOGIC MODELING IN THE SOUTHERN SIERRA NEVADA AND PORTIONS OF THE SAN JOAQUIN VALLEY

Principal Investigators

Jeff Dozier
John E. Estes
David S. Simonett

Contributing Authors

Robert Davis
James Frew
Caryn Gold
Sandra Keith
Danny Marks

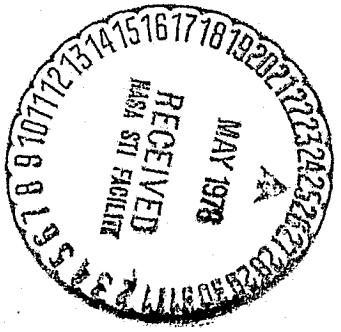

Department of Geography
University of California
Santa Barbara, California
May 1978

Table of Contents

I. Summary of Accomplishments

NASA Grant NSG-5155, "Remote Sensing Applications to Hydrologic Modeling in the Southern Sierra Nevada and Portions of the San Joaquin Valley," was part of a joint US-USSR cooperative project. In addition, the project supported work towards the development of an energy balance snowmelt model for the southern Sierra Nevada.

1. In support of the US-USSR exchange, we have prepared two documents.

   a. A geographical description of the southern Sierra Nevada/San Joaquin Valley test site was sent to the NASA Technical Monitor in June 1977.

   b. A preliminary description of the Soviet test site, the Fergana Valley, was sent to the NASA Technical Monitor in April 1977. In August 1977 we received a translation of the Russian description of the Fergana area, and we have updated our original description to include this new material. This version is included as chapter VI of this report.

2. We have also made some steps toward the development of an energy balance snowmelt model for large basins. This work will be supported in the future by NASA Grant NSG-5062, NOAA, and the University of California Water Resources Center. Therefore we have devoted most of our resources this winter to maintenance of the data collection programs, rather than to development of the models.

   a. We have extended a surface climate simulation model over rugged terrain, and have tested it with soil temperature data from an area in the Wrangell Mountains, Alaska. These data were the most extensive we could find for a mountainous area. A paper on "An Approach toward Energy Balance Simulation over Rugged Terrain" has been submitted for publication, and is included as Appendix 1 of this report.

   b. We have made progress toward the development of a topographic spectral solar radiation model, especially designed for snowmelt modeling. These efforts are described in chapter II, and the data collected are in Appendix 2.

   c. We have made progress toward determination of snow reflectance from Landsat data. These efforts are described in chapter III.

d. Our progress toward a topographic longwave radiation model is described in chapter IV, and the data collected are in Appendix 3.

e. Our investigations into snow-soil heat and moisture flow in the southern Sierra are described in chapter V. Data collected toward this effort are in Appendix 4.

II. Development of a Topographic Solar Radiation Algorithm for Snowmelt Modeling

In high, mountainous areas with sparse vegetation, a major source of energy for snow metamorphism and melt is incoming solar radiation. In such environments melt can take place at low temperatures, even below freezing, and conventional index snowmelt models may perform badly.

Because of the characteristics of snow and of mountainous terrain, a solar radiation algorithm should have the following attributes:

1. It should be spectral, because of the variation of snow reflectance with wavelength.

2. It should account for radiation variations due to slope, exposure, and horizons.

3. It should include calculations for radiation reflected from adjacent terrain.

4. It should be able to make estimates of the required atmospheric attenuation parameters from a limited set of measurements.

5. It should provide for attenuation by clouds.

6. It should be computationally economical.

Thus far our work has been entirely on a clear-sky version of a solar radiation model. For clear-sky conditions we have sufficient data to test our model, but we do not have sufficient cloudy-sky data. The testing of our algorithm is still incomplete; therefore here only the basic structure is presented.

We use the NCIC Digital Terrain Tapes to calculate slope, exposure, and horizon information for any point in a digitized grid. The method is described in detail in a paper by Dozier and Outcalt, which has been submitted for publication, and which is included as an appendix to this report.

A spectral solar radiation model modified from Giergis (1975) is used to estimate beam and diffuse radiation. The variable atmospheric parameters are ozone, precipitable water vapor, and the Beta coefficient in the Angstrom aerosol scattering function. Values for wavelength-dependent ozone absorption are taken from Inn and Tanaka (1953) and Leighton (1961). Water vapor absorption values are taken from Gates and Harrop (1963). Non-variable absorption coefficients for the red molecular oxygen bands (Leighton, 1961) and the near-infrared methane and carbon dioxide bands (Gates and Harrop, 1963) are also included. Values for Rayleigh scattering are taken from Penndorf (1957). The exponent in

the Angstrom aerosol scattering function is assumed to be -1.3, although this assumption can be modified if narrow band spectral measurements are available.

Solar geometry is calculated by standard methods (e.g. Sellers, 1965), and path lengths for air mass and water vapor are calculated by Kasten's (1966) methods. The method for ozone path length calculation is from Lacis and Hansen (1974). We use the values tabulated by Makarova and Kharitinov (1972) for the solar constant.

Diffuse and backscattered radiation are calculated by Giorgis' (1975) method. A provision for specular reflection from adjacent slopes from Paltridge and Platt (1976) is included. However, we have only approximations for the specular component of snow reflectance. Thus this is a source of possible error.

We are now modifying the program so that two measurements, taken at different solar zenith angles, can be used to estimate the necessary atmospheric parameters by solving a set of non-linear algebraic equations using Brown's (1969) method. An earlier approach, whereby we tried to define and measure integrated absorption and scattering coefficients over each Landsat band, proved infeasible, perhaps because the band widths are too large. Hence we have adopted the approach described above, which is independent of the particular wavelength interval of the measuring instrument. A remaining unsolved problem is how to correct for systematic and random measurement errors.

We will use our extensive solar radiation measurements, corresponding to the four Landsat visible and near-infrared bands, taken during the 1977 and 1978 snow seasons, to test our model. These data are included in Appendix 2.

III. Estimating the Shortwave Albedo of an Alpine Snow Cover Using Satellite Radiance Measurements

Introduction

Knowledge of the spatial and temporal variation of shortwave albedo is essential for energy balance computations over an alpine snow cover. Frequent, comprehensive field measurements of surface reflectance over an area the size of the southern Sierra are impractical owing to the area's spatial diversity, extent and relative inaccessibility during the snow season. Derivation of an acceptable estimate of surface reflectance from satellite radiance measurements appears to be the most cost-effective means of completing the shortwave radiation inputs to an energy-balance snowmelt model.

Relevant Characteristics of Landsat MSS Data

1. Spatial characteristics

a. sampling interval: The nominal IFOV of the Landsat MSS is 79 x 79 meters on the ground. Along scan oversampling yields a mean sample spacing of 56 meters in the x-direction. Thus every 15-minute USGS quadrangle (the fundamental unit in our geographic data base) contains well in excess of 10^5 Landsat pixels, which poses a significant computational problem if each pixel is to be evaluated individually. On the other hand, the sampling interval may be sufficiently great that it masks some of the effects of terrain and vegetation on reflectance.

b. areal coverage: Three frames of Landsat imagery are required for complete coverage of the study area. However, less than one-third of any given frame covers an area of interest. Extraction and concatenation of the study area coverage from each frame into a single study area dataset is required, for each frame triplet.

c. distortion: Landsat MSS imagery inherently contains numerous geometric distortions (Van Wie and Stein, 1976; Bernstein and Ferneyhough, 1975) which complicate the assignment of pixel radiance values to specific locations on the ground. Some of these distortions are systematic and may be removed by modeling; others require information regarding spacecraft attitude, altitude, and position which is not directly available to a sufficient level of accuracy, and must therefore be statistically derived with respect to ground control points in the image whose geodetic locations are known. The desired result of these two parallel procedures is a set of mapping transforms relating image and geographic coordinate systems.

2. Radiometric characteristics

a. dynamic range: Landsat MSS data frequently exhibits saturation over snow (McGinnis et al, 1975). Such saturated pixels are essentially useless in radiance calculations. By our own estimates (inspection of threshold shade prints), up to one-third of the most heavily snowcovered areas may saturate in MSS bands 4 through 6. Little saturation seems to occur in Band 7, which is in accordance with laboratory measurements of the spectral reflectance of snow (O'Brien and Munis, 1975).

b. atmospheric effects: Any spaceborne sensor measures a combination of surface and atmospheric radiance. Surface upwelling radiance is subject to selective atmospheric attenuation. The atmosphere itself reflects back into space a portion of the incident solar radiation. The magnitude of this combined attenuation and addition must be calculated for each Landsat MSS wavelength band. In addition, some correction must be made for the change in path length as a function of earth curvature and scan mirror angle.

3. Spectral characteristics

a. identification of snow: Snow has a higher albedo than almost any other phenomenon in the Landsat MSS bands, and thus may be readily identified, except in cases where snow and cloud cover are coincident. It has been demonstrated (Bartolucci et al, 1975) that snow is virtually indistinguishable from clouds in the Landsat MSS bands. A means must be developed to accurately determine which pixels represent snow cover before radiance values are used in further computations.

b. applicability to snow albedo mapping: The Landsat MSS bands span that portion of the spectrum where the albedo of snow exhibits the greatest temporal variation (US Army Corps of Engineers, 1956), and thus requires the most frequent updating for input to an energy-balance model.

4. Temporal characteristics

Landsat's 9-day repeat cycle (combination of Landsats 2 and 3) is far from optimum for snowcover reflectance monitoring. Since the most pronounced changes in albedo occur most nearly following a new snowfall, such a snowfall occurring between overpasses would be quite inaccurately represented, both in terms of areal extent and albedo, by extrapolation from the previous overpass.

Data Collection and Processing

1. Raw data

a. satellite data: Since most of our analysis techniques are digital, we obtain our satellite data as CCTs, for those overpass dates for which we have coincident ground truth measurements.

b. field measurements: Our shortwave ground truth consists of a sequence of measurements at each site using an Exotech 100-A Landsat Ground Truth Radiometer. We have concentrated on the following four field test sites: Cottonwood Pass-Horseshoe Meadow (Kern river basin), Bullfrog Lake-Vidette Meadow (Kings river basin), Bishop Pass (San Joaquin river basin), and Mammoth Mountain (adjacent to San Joaquin river basin). The first three areas are sufficiently remote to preserve relatively undisturbed snow surfaces, yet are accessible in one to two days on skis. The Mammoth area is the location of much present and developing instrumentation by various agencies in cooperation with the ski area management. All four areas are easily located on Landsat imagery and have measurement sites which are relatively free of topograhic effects.

c. topographic data: We have developed software to extract 15-minute quadrangles from NCIC Digital Terrain Tapes, and resample them to any desired spatial resolution. The quadrangles from the fundamental grid of our study area database, and all Landsat and field measurements are located with respect to the terrain grid.

d. ground control data: Ground control points are located on both USGS 15-minute quadrangle maps and on line printer shade prints of the Landsat imagery. We are in the process of implementing a digital video display method of identifying control points in the image.

2. Simulated data

a. atmospheric parameters: Atmospheric path radiance and transmissivity are calibrated with radiometer field measurements, then simulated by a model described elsewhere in this paper.

b. solar irradiance at the surface: Beam and diffuse solar radiation are simulted using a combination of the atmospheric model, terrain data, and an ephemeris program which we have developed.

3. Data processing

The principal data processing problem is the precise location of field measurement sites on the Landsat CCTs. This has been partially alleviated by selecting test sites that are uniform and extensive enough so that a moderate locational error (eg, < 2 pixels) will still yield acceptable results. For areas where topographic effects are important, however, the positional error must be less than one pixel.

We are currently performing image rectification using the DIRS program suite developed at GSFC. This has proven unsatisfactory for three reasons. First, the program runs in a batch mode, which leads to unacceptably long turnaround times on a heavily-used educational system, especially when generating shade prints for GCP location, which requires a special configuration of our system's line printer. Second, the programs are poorly documented, difficult to modify, and produce cryptic output and diagnostics. Third, the programs are collectively quite expensive on our system configuration (for example, reformatting and deriving mapping functions costs about $200 in computer time alone). We have thus begun implementing a cut-down, highly specialized rectification program on a minicomputer (PDP-11/45) which has significantly more online disk storage (600 Mbytes) and an interactive operating system (UNIX).

A secondary data processing problem, which is relatively straightforward, is the conversion of the Landsat radiance numbers to surface upwelling radiance, using a combination of a table lookup and the atmospheric model.

Initial Verification

Although both Landsat and field data are available for several dates during 1976-77 snow season, a preliminary calculation of albedo based on space measurements has not been attempted for the following reasons:

1. The initial version of the atmospheric model contained numerical instabilities which necessitated its being redesigned, which is still under way.

2. Several errors were discovered in the field radiometer measurements, necessitating a statistical filtering of the recorded values.

3. The image rectification programs were initially run on a summer image, to facilitate location of control points in the study area. We have had difficulty registering a winter image to the rectified summer image. The programs we are using also do not readily rotate imagery so that it is aligned to the cardinal directions, as are our terrain datasets and USGS maps.

We feel that these errors have been remedied by moving to a new computer environment, developing a new atmospheric model, and recalibrating our field instruments.

Once we are satisified that we can compute snow albedo over a uniform snowpack, we will attempt to extend the model over a topographic surface, which may necessitate corrections for the high specular reflectance which snow exhibits at low sun angles (Dirmhirn and Eaton, 1974). Areas where this is a problem may be readily identified by combining the ephemeris calculations (program) with slope and aspect information derived from the terrain tapes. Existing numerical corrections for anisotropic reflectance (eg, Middleton and Mungall, 1952) require some knowledge of the physical characteristics of the snowpack which may be difficult to obtain from either remote sensing or field measurements.

IV. Development of a Technique for Modeling Incoming Longwave Radiation in Mountainous Terrain

One of the most important parameters considered in the energy balance of a snowpack is incoming thermal radiation from the atmosphere and surrounding terrain. This is a difficult parameter to measure over an area, especially in mountainous terrain. It must be modeled very carefully to get meaningful results. There are typically large diurnal variations and complications are caused by cloud cover, forest cover, and surrounding slopes.

Longwave radiation is important in the energy budget of a snowcover because of the combined effects of the absorption characteristics of snow in the thermal region and the attenuation characteristics of the atmosphere. Thermal radiation exchange with a snow cover is contingent upon three important considerations:

1. Snow is a near perfect absorber of thermal radiation, while being a good reflector of solar radiation (US Army Corps of Engineers, 1956; Kondratyev, 1973).

2. Cloud cover substantially affects the surface radiation balance by reducing incoming solar radiation and by increasing incoming thermal radiation. This is especially important in high alpine areas where extensive cloud cover is likely during the snow season.

3. Thermal radiation exchange occurs during both day and night.

In order to realistically deal with the above considerations, the longwave radiation model should have the following characteristics:

1. It should compute the variations in atmospheric emissivity with elevation and time of day.

2. It should account for the effects of surrounding slopes in terms of both horizon effects and thermal radiation of these slopes.

3. It should account for the effects of cloud cover and forest cover on surface thermal exchange.

4. The model should be driven by a limited set of discontinuous surface measurements.

Work to date on the longwave radiation model has been limited to clear sky conditions and does not include corrections for forest cover effects. The assumption of a homogeneous snowcovered surface is made. The model has not

been completely tested at this time; though sufficient data have been collected (see Appendix 2). The general structure of the model is presented in the following section.

1. The study area is divided into a grid using the NCIC Digitial Terrain Tapes in a mannner described by Dozier and Outcalt (Appendix 1). Measurements of air temperature and vapor pressure at various times and elevations are then interpolated to this grid using a lattice-tuning method and a bi-cubic spline interpolation. A temperature and a vapor pressure is then stored for each cell in the time/elevation matrix. This information is then used to compute a temperature and vapor pressure for each grid point at each time step of the model.

2. Thermal emission from the atmosphere is principally a function of the water vapor, carbon dioxide, and ozone contents (Paltridge and Platt, 1976). Brutsaert (1975) developed a technique whereby atmosphereic emissivity can be determined from near surface vapor pressure and air temperature measurements, eliminating the need for vapor pressure and temperature profiles or soundings. This technique is modified for the non-standard atmospheric conditions encountered in alpine areas. Corrections are made for both pressure variations, and temperature and vapor pressure lapse rates, which are determined from field measurements. Atmospheric emissivity is then computed for each grid point for every time step of the model.

3. Using horizon information previously computed (as discussed earlier), a thermal view factor is computed for each grid point, using techniques developed by Reifsnider and Lull (1965), and Lee (1972), and modified by Dozier and Outcalt (Appendix 1).

4. Incoming longwave radiaton from the atmosphere and surrouding slopes is then calculated for every grid point from the previously described information for a variety of time steps. The incoming longwave radiation matrix is then stored for later input to the snowmelt model, and plotted as surface contour maps over the study area.

Possible Errors and the Need for Further Work

The weaknesses of the model lie in its simplifying assumptions and in data measurement errors. The exclusion of cloud cover and forest cover parameters is responsible for most model errors. As reliable data becomes available on these parameters they will be included in the model. Vapor pressure data derived from wet bulb temperature is

particularly unreliable at or around 0° C due to energy released during phase change. A more reliable method for determining vapor pressure will be explored. Surface temperature of surrounding slopes, used in Step 3 above are generally poor estimates of reality. No account is made for slope or exposure differences and the actual measurement of the surface temperature is probably unreliable. Better techniques for measuring this parameter, possibly using thermal imagery, must be developed. In general a few sites where continuous measurements of all of the input parameters could be collected would greatly enhance the model's reliability.

V. Snow-Soil Heat and Moisture Flow in the Southern Sierra

The literature review on soil heat and thermal processes has been essentially completed. Methods have been determined for estimating the various soil thermal and hydraulic parameters required for input to soil heat-moisture transfer models. Various models have been surveyed and have been found to be both mathematically complex and therefore computationally expensive and partially inappropriate for the conditions under which the model will be used.

Generally the literature has indicated that for the relatively coarse soils of the Southern Sierra a model of the soil-snow heat and moisture exchange should have the following attributes:

1. The model must be able to calculate heat flow by conduction with various surface boundary layer conditions simulating diurnal and seasonal changes.

2. The model should account for downward percolation of meltwater, cooling the soil and thereby ameliorating upward heat transfer to an overlying snowpack.

3. The model must adequately simulate the transfer of heat due to upward diffusion of water vapor, counter to the downward percolation of meltwater.

4. The model must also be useful in determining the formation of frost, the degree of ice segregation and the degree of ice saturation with given initial conditions, in order to evaluate the efficiency of meltwater runoff.

5. The model must yield, as output, predicted temperature and moisture content at various depths within the soil as well as an estimation of the total snow-soil heat and moisture exchange. This allows testing and calibration using in situ measurements.

6. The model must be compatible for use as a subroutine to the snowmelt model and its coupling to a hydrologic flow model.

Many of the surveyed soil models require common input parameters. Measurement and estimation of soil properties for input into soil heat-moisture transfer models are presently underway. Samples obtained from the thermistor/soil moisture block sites are used in these procedures.

Soil Physical Properties

Textural and structural analyses of six soil samples have been performed using standard sieve-weight partitioning. These analyses determine the textural and structural character, both important for the estimation of thermal and moisture properties. The amounts of clay and silt fractions in the various samples have been sufficiently low such that particle size analysis of these fractions using differential settling methods has not been used. In addition to the standard textural and structural analyses, mineralogical and predominant particle shape information has been gathered using a standard binocular petrographic microscope with grain count grids.

The previously described measured soil propeties are used in the calculation of soil porosity, bulk density, optimum moisture content and other parameters. These are used in the estimation of soil thermal and moisture properties.

The soil thermal conductivity and heat capacity will be estimated by two methods. Texture, mineralogical composition, and particle-shape distribution of the various samples will be used as input to the material fracton model employed by Philip and DeVries (1957) to estimate these properties. These estimates will be compared with the experimental values of thermal conductivity and heat capacity for similar soils as determined by Kersten (1949). The temperature dependence of thermal conductivity and heat capacity due to the presence of unfrozen water in the fine separate of soil (Penner, 1970) is neglected in the calculations with our soil samples due to the low quantity of fines present. However these parameters do effectively change with liquid water and ice content (Nixon and McRoberts, 1973).

The hydraulic properties of the soil samples will be determined using textural and particle shape information with the appropriate moisture characteristic and desorption curves. Outcalt (1976) specified log-log fit parameters to abstract the shape of both the desorption and the unsaturated hydraulic conductivity curves. Soil porosity was used with these parameters to establish the relationships between the hydraulic head, the unsaturated hydraulic conductivity and the water volume content. These input values can also be used to describe the thermal flow as well since it is coupled with the moisture transfer. Green and Corey (1971) have reviewed various methods of calculating unsaturated hydraulic conductivity using soil pore-size distributuion solely. They concluded that all of the reviewed methods adequately predicted experimentaly measured values for a range of soil types. To obtain estimations for the soils of the Sierra Nevada, more than one method will be used to calculate each of the soil hydraulic properties.

Field Measurements

During the summer and fall, 1977, field temperature and moisture measurement sites were established in the test area. The locations of the test sites were chosen on the basis of ease of access, location of the Cooperative Snow Survey snow courses, and the representativeness of the location.

Seven thermistors and six soil moisture blocks were installed at each site at various depths. These were selected to correspond to textural or composition changes observed during the installation. In some sites a total depth-range sample was prevented due to difficulty in digging holes. At two sites, two soil moisture blocks were assigned to each depth with separate holes. At the other sites all six of the moisture blocks were installed at various depths. There were three thermistors placed within the soil at each site at depths corresponding to those of some of the moisture blocks. During the installation soil samples were obtained from the appropriate depths, and a preliminary field description was done.

Since the test sites were established each site has been visited during the snow season to obtain in situ measurements of soil and snow temperature and soil moisture content (see Appendix 4).

Soil Moisture Block Accuracy

The soil moisture blocks measure resistance across stainless steel grids implanted in fine-textured plaster-of-paris (gypsum) blocks. The moisture measured is transferred from the surrounding soil into the block by the capillary suction of the block material. The resistance measured directly corresponds to the moisture content in terms of percentage of available water for unfrozen conditions. Although it is reasonable to assume that the block measurements are accurate due to the textural contrast between the block and the surrounding soil for unfrozen conditions, it has been shown that the block resistance increases greatly when freezing occurs (Sartz 1967, 1970). Also it is expected that the soil water system would freeze and thaw sooner than the block water system due to their respective textures. In order to calibrate the block measurements during freezing, other moisture sensors have been obtained with different construction. These sensors operate on the same principle as the blocks, but consist of a sandwich of stainless steel and fiberglass. The porosity and permeability of these sensors is similar to that of the soil. These sensors contain built-in thermistors and may be oriented such that they are most sensitive to vertical moisture movement. They will provide control data for comparative use with the soil moisture block data.

References for Chapters I-V

Bartolucci, L.A., Hoffer, R.M., Luther, S.G., 1975. Snowcover mapping by machine processing of Skylab and LANDSAT MSS data. Workshop on Operational Applications of Satellite Snowcover Observations, ed. A. Rango, Lake Tahoe, 269-285.

Bernstein, R., Ferneyhough, D.S., Jr., 1975. Digital imaging processing. Photogrammetric Engineering and Remote Sensing, 41, 1465-1477.

Brutsaert, W., 1975. On a derivable formula for long-wave radiation from clear skies. Water Resources Research, 11, 742-744.

Dirmhirn, I., Eaton, F.D., 1975. Some characteristics of the albedo of snow. Journal of Applied Meteorology, 14, 375-379.

Gates, D.M., Harrop, W.J., 1963. Infrared transmission of the atmosphere to solar radiation. Applied Optics, 2, 887-897.

Georgis, R.B., 1975. A simple solar radiation model for computing direct and diffuse spectral fluxes. M.S. Thesis, Department of Atmospheric Science, University of California, Davis.

Green, R.E., Corey, J.C., 1971. Calculaton of hydraulic conductivity: A further evaluation of some predictive methods. Proceedings of Soil Science Society of America, 35, 3-8.

Inn, E.C., Tanaka, Y., 1953. Absorption coefficient of ozone in the ultraviolet and visible regions. Journal of the Optical Society of America, 43, 870-873.

Kasten, F., 1966. A new table and approximation formula for the relative optical air mass. Archiv fur Meteorologie, Geophysik und Bioklimatologie, ser. B, 14, 206-223.

Kersten, M.S., 1949. Laboratory research for the determination of the thermal properties of soils. Final Report, Engineering Experimental Station, Minnesota University, Minneapolis, Minnesota.

Lacis, A.A., Hansen, J.E., 1974. A parameterization for the absorption of solar radiation in the earth's atmosphere. Journal of the Atmospheric Sciences, 31, 118-133.

Lee, R., 1962. Theory of the 'equivalent slope'. Monthly Weather Review, 90, 165-166.

Leighton, P.A., 1961. Photochemistry of Air Pollution. Academic Press, New York.

Makarova, Ye.A., Kharitinov, A.V., 1972. Distribution of energy in the solar spectrum and the solar constant. NASA TT-F-803.

McGinnis, D. F., Jr., McMillan, M.C., Wiesnet, D.R. Factors affecting snow assessment from LANDSAT data. NASA Earth Resources Survey Symposium, I-D, 2661-2668.

Nixon, J.F., McRoberts, N.R., 1973. A study of some factors affecting the thawing of frozen soils. Canadian Geotechnical Journal, 10, 444-445.

Outcalt, S.I., Carlson, J.H., 1975. A coupled soil thermal regime surface energy simulator. Conference on Soil-Water Problems in Cold Regions, Calgary, 1-32.

O'Brian, H.W., Munis, R.H., 1975. Red and near-infrared spectral reflectance of snow. Workshop on Operational Applications of Satellite Snowcover Observations, ed. A. Range, Lake Tahoe, 319-334.

Paltridge, G.W., Platt, C.M.R., 1976. Radiative Processes in Meteorology and Climatology. Elsevier Scientific Publishing Company, Amsterdam and New York.

Penndorf, R., 1957. Tables of the refractive index for standard air and the Rayleigh scattering coefficient for the spectral region between 0.2 and 20.0 microns and their application to atmospheric optics. Journal of the Optical Society of America, 47, dddddd 176-182.

Penner, E., 1972. Thermal conductivity of frozen soils. Canadian Journal of Earth Sciences, 7, 982-987.

Philip, J.R., DeVries, D.A., 1957. Moisture movement in porous material under temperature gradients. Transactions of American Geophysical Union, 38, 222-232.

Reifsnyder, W.E., Lull, H.W., 1965. Radiant energy in relation to forests. US Forest Service Technical Bulletin 1344.

Sartz, R.S., 1967. A test of three direct methods of measuring depth of frost. Soil Science, 104, 273-278.

Sartz, R.S., 1970. Natural freezing and thawing in a silt and sand. Soil Science, 109, 1314-23.

Sellers, W.D., 1965. Physical Climatology. University of Chicago Pres, Chicago and London.

Van Wie, P., Stein, M. A Landsat Digital Image Rectification System. Goddard Space Flight Center, Greenbelt, Maryland.

VI. Geographic Description of the Fergana Area

Introduction

This study provides a basic geographic description of the Fergana Valley in the South Central USSR, with emphasis on the Soviet study area, part of the joint US/USSR cooperative research program, which includes the basins of the Gavasay, Sumsar, Kassansay and Padshaata Rivers. It contains information provided by the Soviet Union on the study area, as well as information contained in earlier progress reports.

Soviet Central Asia is part of a vast synclinal depression between the Russian and the Central Siberian Platforms. Rolling plains, typical of the region, are made distinctive by the effects of a desert climate, while the southern rim is accented by the Pamirs, the highest mountains in the USSR. The Fergana Valley (Ferganskaya Dolina), a large intermontane synclinorium, lies in the central eastern part of Soviet Central Asia (Figure 1), just north of the Pamirs. The Kuramin and Chatkal mountains (both part of the Tien Shan Range) bound it to the north, the Alai and Turkistan to the south, and the Fergana Mountains to the east (Figure 2). The floor of the valley, sloping from east to west, is separated from the foothills of the surrounding mountains by a series of well-developed alluvial fans. Flowing westward along the northern edge of the valley is the Syr Darya. South of the Syr Darya is an area of relatively level land covered by sand dunes, salt marshes, and salt lakes. A large alluvial fan at the southwestern end of the valley was formed by sediments deposited by the swift-flowing Sokh River, which disgorges into the valley from the mountains in the south. A zone of springs and wells occurs around the perimeter of the alluvial fan between the 450 and 400 m contours (Plummer, et al, 1971). On the west is the narrow (8 km wide) Leninabad Pass, through which the Syr Darya flows, joining the Fergana Valley to the Golodnaya (Hungry) Steppe. The Soviet study area, in the north-central portion of the valley, is bounded by the Kuramin Range to the west, and by the Chatkal Range to the north and east. Rivers which supply the Syr Darya drain the southern slopes of these mountains (Figure 2).

The Fergana Valley is at roughly 40° to 42° N latitude, approximately the latitude of Denver, Colorado, USA (Figure 3), with a longitude of 70° to 73°. The valley is in the form of an ellipse, 300 km long and 150 km wide, with an area of approximately 22,000 sq km. The surrounding mountains reach an elevation of nearly 6000 m in the south and 4500 m in the north, while the surface of the valley rises from 300 to 400 m in the west (Leninabad is at 325 m) to 500 m at Andizhan in the eastern end, and 900 to 1000 m in the southeast (Osh, in the foothills, is at 990 m) (Suslov, 1961). Namangan, in the north, is at 440 m, and

Fergana, in the south, is at 580 m. The surface of the valley is fairly level, the central part of which is desert. Salt playas, for the most part dry, but flooded in some years by high river water, are characteristic of this central region, as are salt-marsh swamps, such as the Dam-Kul, which are in the process of drying out (Suslov, 1961).

The Fergana Valley lies mainly in the Uzbek SSR and partly in the Tadzhik and Kirgiz SSR's (Figure 4). (The intricate boundary delineation in the area stems from an effort to include the mountain watershed areas with the parts of the basin to which they supply water, and considerations of different nationality groups). Although Uzbekistan contains only one-third of the total area in Central Asia, the Fergana Valley provides it two-thirds of the population, three-fourths of the industrial output, and over one-half of the arable land.

The Fergana Basin (Figure 5) has the highest population density and the highest concentration of agriculture and industry in Uzbekistan (Gregory, 1968). The foothill ring is the most densely populated; here there is a continuous belt of cultivated, irrigated land which receives water from numerous mountain streams. This large population concentration in a small area contrasts with the large and virtually uninhabited desert and semi-desert areas of most of Soviet Central Asia (Allworth, 1967). Most of the Fergana Valley is characterized by a rather dense rural population of more than 50 persons per sq km, rural population making up 60% or more of the total population of the valley (CIA, 1974). However, the western end of the valley, in the Kokand region, has a rural population of only 1 to 10 persons per sq km. The largest cities in the valley are Andizhan (173,000), Namangan (164,000), Kokand (133,000), Fergana (111,000), and Margelan (89,000). Kuvasai and Leninsk have populations of 30,000 to 100,000. Several cities along the southern edge of the valley have populations of 10,000 to 30,000, with many smaller cities of less than 10,000 (Burikin, 1967). The quantity of water that is available partly explains the density of villages located on the lower elevations of the alluvial fans and on the numerous distributaries of the major rivers (Plummer, et al., 1971).

The vegetation of the Fergana Valley (Figure 6) forms a series of belts, or rings, surrounding the central Fergana desert and extending into the foothills and mountains surrounding the valley. The nature of the plant cover of this territory varies widely in relation to the local elevation, slope exposure, and rainfall distribution. Several main vegetative belts can be distinguished: 1) desert, 2) steppe, 3) mountain-meadow, alpine and subalpine, 4) forests, thin-forests, and scrub, and 5) rocky ridges, mounds, moraines, and firns with sparse vegetation.

The vegetation of the foothill desert is mainly represented by ephemerals, sometimes in community with wormwood and Russian thistle. Wormwood is found on the alluvial fans and into the foothills. A typical feature of ephemeral vegetation is the fact that it develops only in the wet autumn period and especially in the spring period, when the grass stand is continuous, even though short-lived (30-40 days). With the cessation of the spring rains, the above-ground part of the ephemers rapidly dries up and the locale changes into a sun-scorched gray-yellow desert with individual bushes of wormwood or Russian thistle, carpeting only 30-40 percent of the ground.

Steppe areas are characterized mainly by drought-resistant vegetation represented by various cereals and some spring-autumn ephemers.

Mountain meadows are chiefly composed of "mesophytes", which require year-round precipitation for their growth. These meadows are found at elevations of 1500-1300 m. The grass stands typically grow to 1 m and 80-90 percent of the soil is covered by vegetation.

Subalpine vegetation is found at elevations of 3000-3500 m. Grass stands are dense, covering 85-90 percent of the soil, and it is 35-50 cm high.

Alpine meadows have the highest location (3200-4000 m) and are represented by motley grass-cereal and sedge meadows. The height of grass stands here are 25-35 cm and the soil is 50-80 percent covered by the vegetation.

Forests, as commonly understood, are scattered in small sections. Spruce, spruce-fir, juniper, and nut-bearing forests are most common. Among the trees are found an understory with infrequent clusters of spirea, dog rose, and honeysuckle.

Rocky sections of ridges and slopes, mounds, and Recent moraines at the highest altitudes have sparse plant cover. This zone has roughly the same appearance over the entire territory described.

Table 1 lists the distribution of vegetative types, by percent area, in the test site basins.

Figure 1. The Fergana Valley in respect to Soviet Central Asia and the USSR (from CIA, 1974).

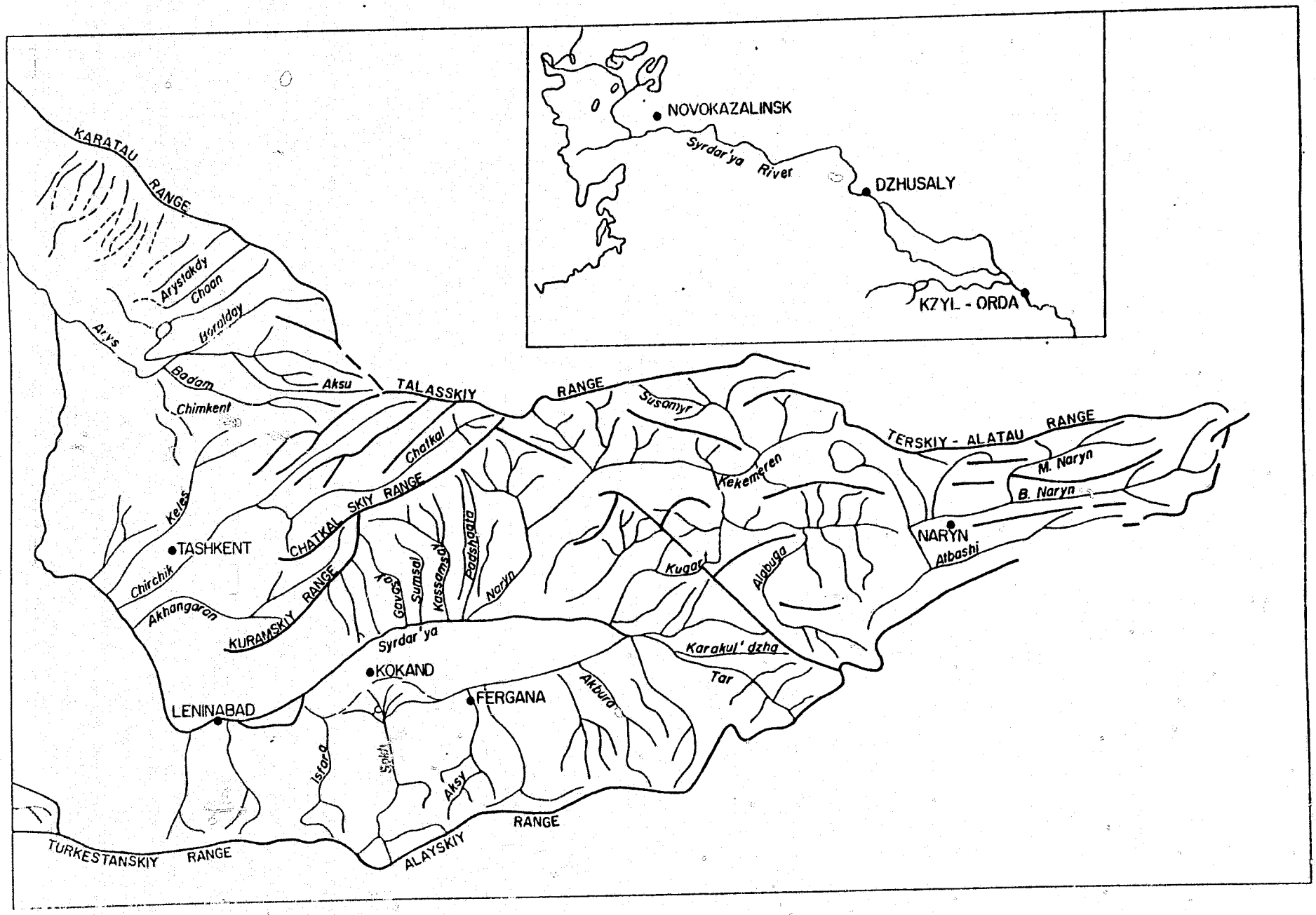

Figure 2. Drainage of the Fergana Valley

Figure 3. Comparative area and latitude of the US and USSR (from CIA, 1974).

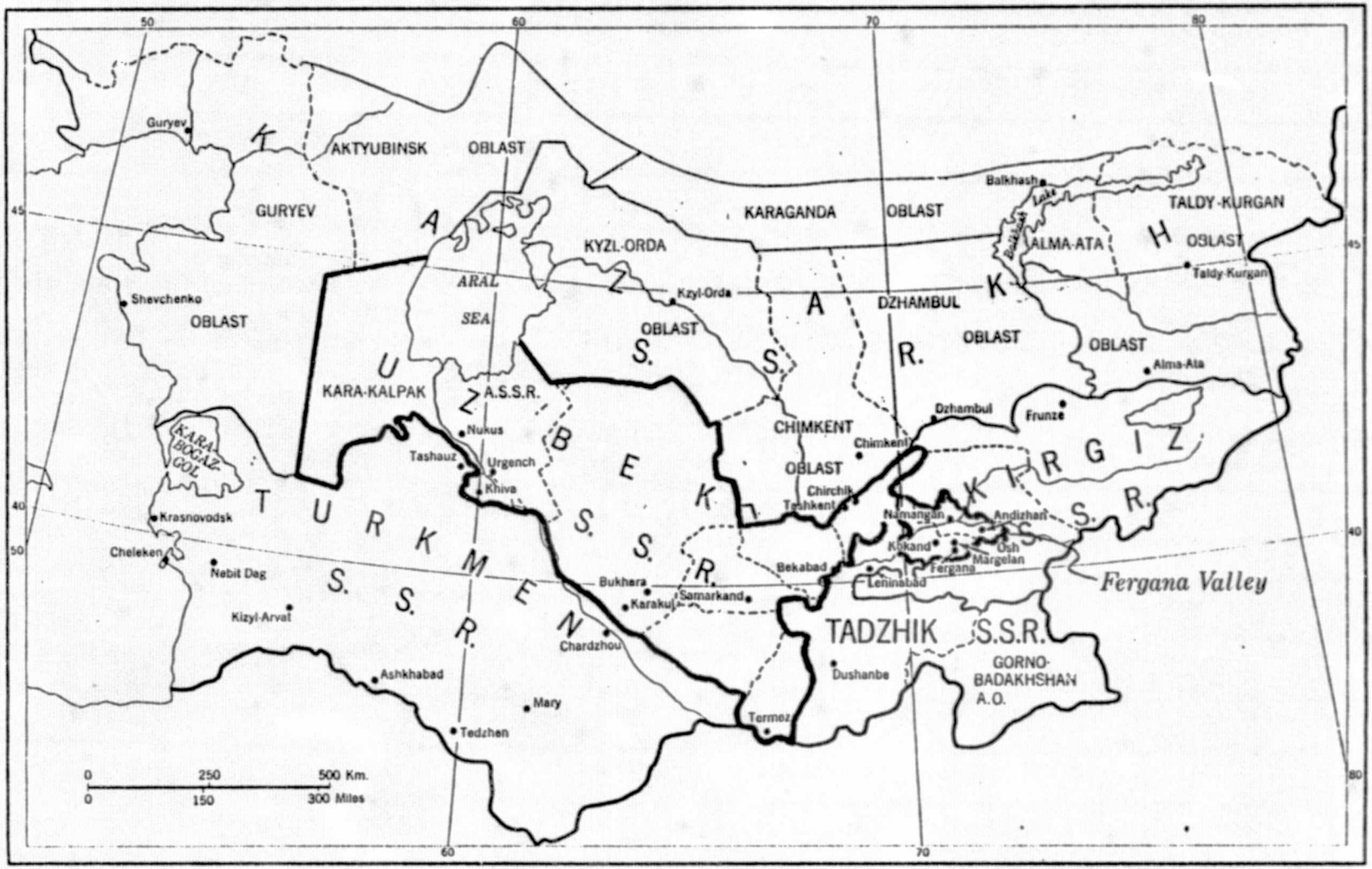

Figure 4. Fergana Valley, Uzbek SSR (from Lydolph, 1970).

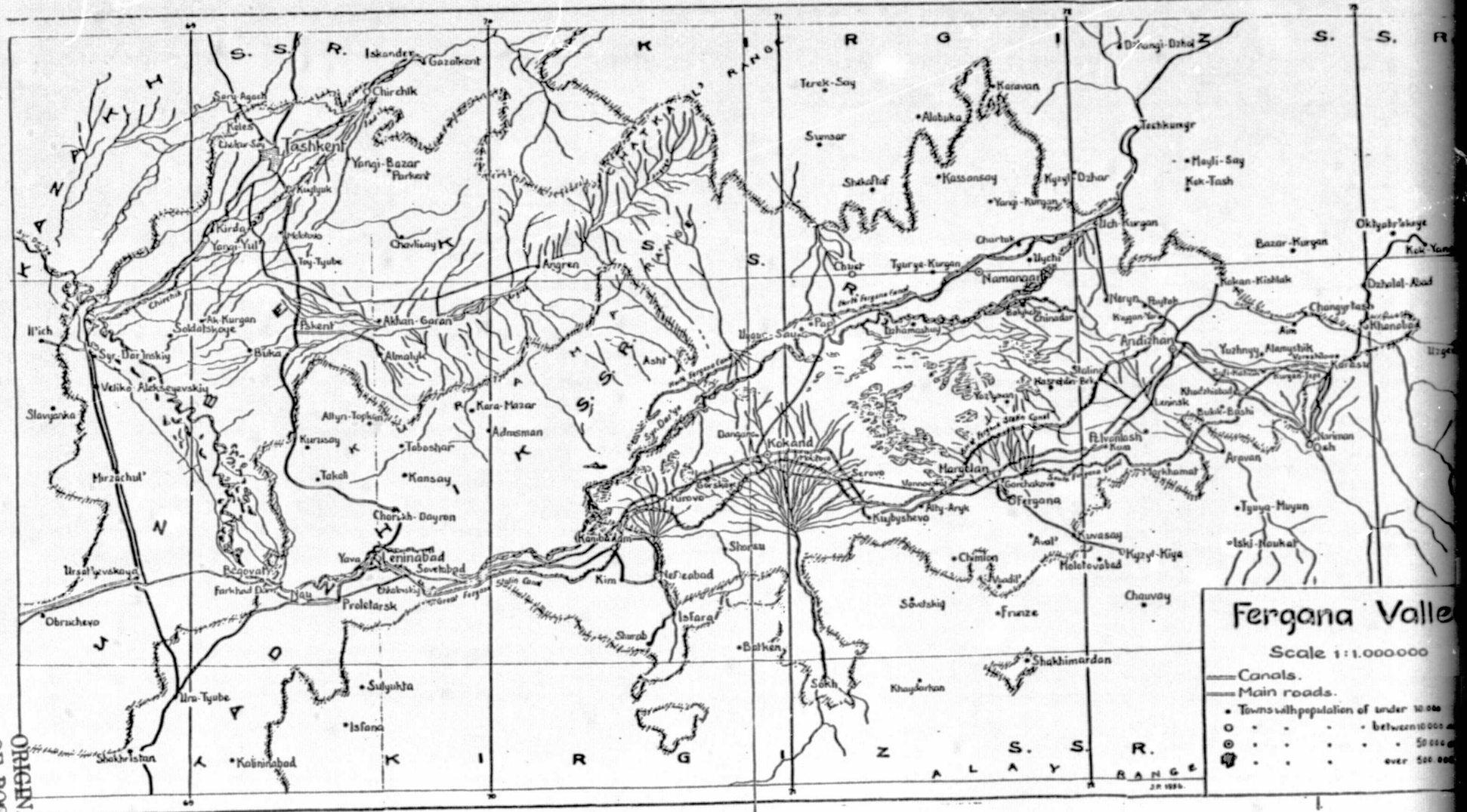

Figure 6. The Fergana Valley, Uzbek, SSR (from Wheeler and Footman, 1954).

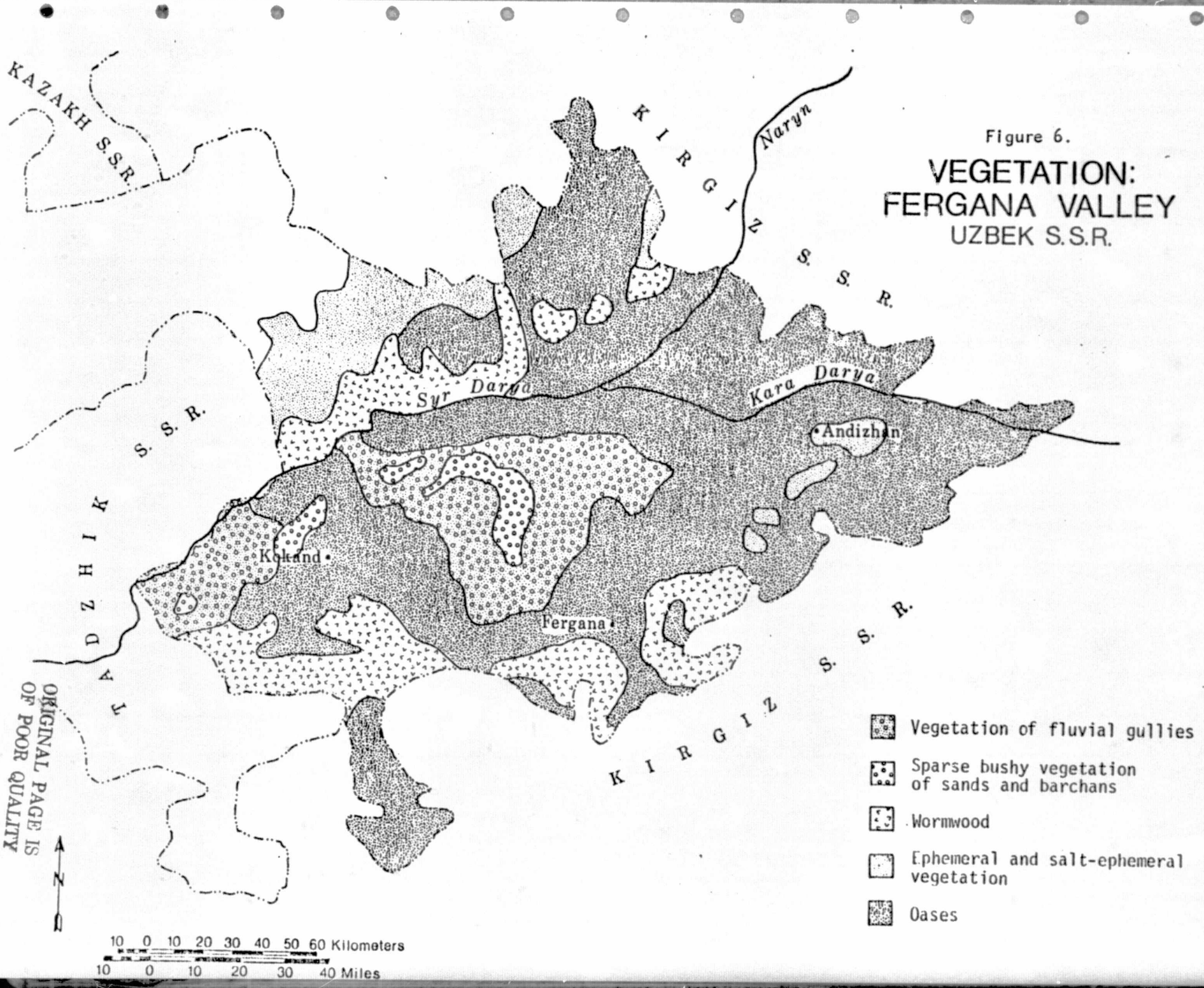

Figure 6.

VEGETATION: FERGANA VALLEY UZBEK S.S.R.

	BASIN AREA km²	LITHOLOGIC ROCK COMPLEXES			SOIL COVER				VEGETATION				
		Semiloose Rocks of Mesozoic Paleogenic & Neogenic Ages; Rocks with Fissured Type of Water Permeability	Carbonate & Hydrochemical Paleozoic Rocks Fissured-Karst Type of Permeability	Metamorphic & Igneous Rocks; Fissured Type of Permeability	Serozem	Brown & Chestnut Soils	Light-Brown Soils & Alpine Meadow Steppes	Light-brown Meadow-Steppe Alpine Soils Eroded, Coarsely Skeletal Among Bedrock Outcroppings	Deserts	Steppes	Mountain-Meadow Alpine & Subalpine	Forests Thin Forests & Scrub	Rocks, Mounds & Moraines With Sparse Vegetation
Padshaata Mouth of Tostu River	366	22	78	--	--	38	22	40	--	61	--	20	19
Kassansay Mouth of Uryukty River	1240	8	7	85	6	43	51	--	10	26	48	10	6
Gavasay, Mount of Ters River	361	--	5	95	--	40	60	--	--	35	7	58	--
Gavasay, Gava-kishlak Village	657	--	4	96	11	53	36	--	15	26	4	55	--

Table 1. Rock complexes, soil cover and vegetation of test area basins (by percent area)

Climate

The Fergana Valley lies in a semi-arid region with cold winters and dry, hot summers. The Koppen-Gieger climate classification for the region falls in the boundary zone between a dry, cold, desert (BWk) and a dry, cold steppe (BSk) (Strahler, 1974). The Koppen System classifies the desert regions of Nevada-Utah in the western United States and the Atacama Desert in Chile as having similar climates. This comparison is deceptive. The climate of the Fergana must not be viewed on a macroscale, but a more meso or micro level to fully understand the impact of climate on the valley's agricultural and industrial productivity.

The two most important physicgraphic factors in the climate of the Fergana Valley are its continental location and the surrounding mountain ranges. The valley's geographic location basically removes any marine effect and produces relatively extreme temperatures in all seasons. The surrounding mountains modify this somewhat by providing a rain shadow effect in some seasons and intense orographic conditions in others. In addition, the surrounding mountains give the Fergana Valley a more mild climate than it might have, although snow and frost do occur in the valley proper in December and January, when the temperature may fall as low as -15°C. At Tashkent, a first order weather station about 80 miles northwest of Leninabad and outside the Fergana Valley itself, temperature variations are much more extreme. This may be seen in the mean monthly temperatures, averaged over the period 1951 to 1960, shown in Table 2. Figure 7 shows climographs of Fergana, Namangan, and Osh (Walter and Leith, 1967).

Soviet Central Asia is basically under the influence of travelling westerly air masses, with the cyclo- and anticyclogenesis intrinsic to it. Also quite important are cyclones, moist westerly air masses, and cold northerly air masses, lowering air temperature and causing precipitation. The relative abundance of spring and winter precipitation is caused by cyclonic storms from the Mediterranean and Black Seas. In summer, the air is too dry for precipitation in spite of orographic currents. The mountains to the south provide a barrier producing a rain shadow effect from the monsoon of Southern Asia (Suslov, 1961).

Owing to the diversity of slope exposure with respect to the moisture-bearing air masses, precipitation varies throughout the region. The mean-annual precipitation totals fluctuate from 80-100 to 400-750 mm. (Resources of Surface Waters of the USSR, 1969)

The smallest annual precipitation totals are observed in the Gavasay River basin, occupying the most westerly position in the study area. As one moves eastward, precipitation increases and reaches maximum values in the Padshaata River basin. On the southeast slopes of the

Chatkal range little precipitation falls. In the valleys of the Gavasay and Kassansay rivers, at 1000-1800 m, the total precipitation each year does not exceed 300 mm (Resources of Surface Waters of the USSR, 1969). Heavy precipitation falls on the east side of the Chatkal range. In the Padshaata River basin, at 1500 m elevation, the annual average is 700 mm; and near the crests of the mountains, the average is 1000-1200 mm. Figure 8 shows the distribution of annual precipitation totals with elevation in this region. In the foothill and low-mountain zones, most precipitation occurs in winter and spring (Figure 9); summer and autumn are dry. Table 3 gives mean monthly precipitation and water balance data for Tashkent, Fergana, Andizhan and Namangan.

Compared with the foothills, precipitation totals are more evenly distributed throughout the year in the mountain regions. At about 2000 m there is little difference between summer and winter precipitation totals.

In most cases, in the mountain region, the number of days with precipitation goes up with a concommitent increase in precipitation totals: the mean annual number of days with precipitation in this region is 100 to 150 days.

Some years, precipitation in the form of rain showers occur five to seven times a year in the basins of the Padshaata and Kassansay rivers. The showers may last 20-25 hours. Maximum shower intensity varies from 0.10 to 1.80 mm/min or higher. In June 1957, the maximum shower intensity in the Kassansay River basin reached 3.1 mm/min (Resources of Surface Waters of the USSR, 1969).

Owing to the geographic positon, this region gets a relatively large amount of solar energy, especially in summer. The influx of solar radiation in the foothill part of the basin in a year's time is about 140 kcal/cm^2 (Handbook on Climate in the USSR, 1973). With increased elevation, owing to a reduction in the density and dust content of the air, the total influx of radiation rises to 150-155 kcal/cm^2 (Handbook on Climate in the USSR, 1973). The largest mean-monthly levels of total radiation are about 20 kcal/cm^2 and occur in June and July. The smallest radiation influx is observed everywhere in December; it is 4-7 kcal/cm^2 (Handbook on Climate in the USSR, 1973).

Annual levels of net radiation change over the territory from 48 to 50 kcal/cm^2 (Spravochnik po klimatu SSSR, 1973). The largest total monthly levels (8-11 kcal/cm^2) occur in June and July (Spravochnik po klimatu SSSR). Net radiation is lowest in December and January, when it drops to 0.3-0.5 kcal/cm^2.

The relationship of evaporation with local elevation is manifested quite clearly. The amount of evaporation depends primarily on climatic factors; mainly precipitation and

relative humidity. The latter decreases abruptly with elevation in the mountains. A graphic presentation of the decrease in vapor pressure with elevation is given by Figure 10. Because precipitation increases with elevation (to a certain point) evaporation also initially increases with elevation; at higher elevations, however, it decreases (Shul'ts, 1965). In the valley proper, in summer, clear skies and dry sukhovey winds from the southeast can cause evaporation which may exceed annual precipitation by many times.

In the mountainous part of the basins, air temperature decreases with elevation. For example, at elevations to 1200 m the mean daily air temperature in January is from -2 to -5°; at 1200-2000 m, -3 to -7°; and in the 2000-3000 m zone, the mean daily air temperature drops to -8 to -9° (Resources of Surface Waters of the USSR, 1969). July and August are the hottest months. The highest mean daily temperatures are observed in the foothills (26-28°). At the elevations of 2000-3000 m it does not exceed 10-20°. In the high-mountain zone night frosts are common in summer.

In winter, on the slopes of the Chatkal range the adiabatic lapse rate ranges from 0.27 to 1.4°, and in summer gradients range from 0.11 to 0.73° (Resources of Surface Waters of the USSR, 1969).

Table 2. Mean Monthly Temperatures for Tashkent, 1951-1960

	°C	°F
January	.9	33.6
February	2.8	37
March	6.3	43.3
April	14.3	57.7
May	19.5	67.1
June	24.5	76.1
July	26.9	80.4
August	24.8	76.6
September	19.5	76.1
October	12.4	54.3
November	5.3	41.5
December	1.2	34.2
Mean	13.2	55.8

(from World Weather Records, 1967)

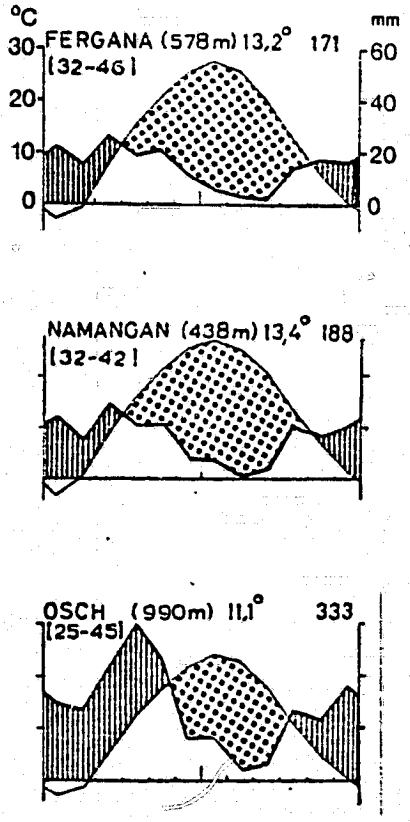

Figure 7. Climographs of Fergana, Namangan, and Osh (Osch) (from Fetisova, 1965).

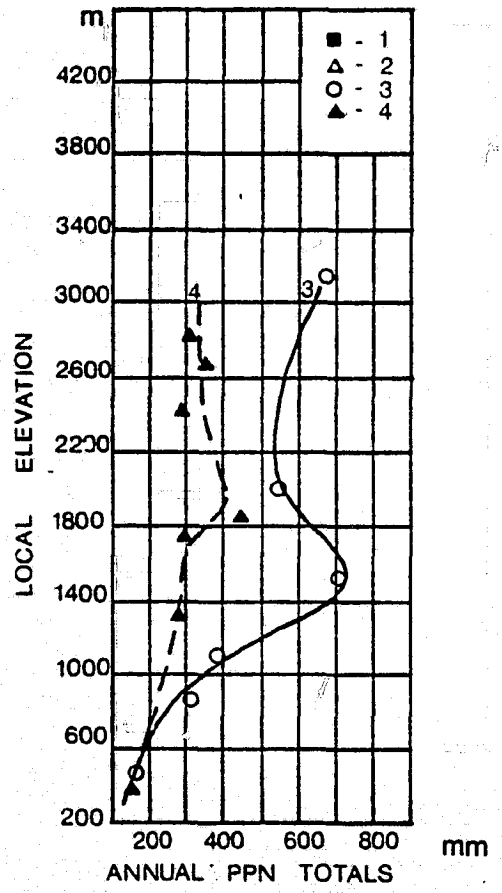

Figure 8. Variation of precipitation with elevation

3 - Padshaata River

4 - Gavasay River

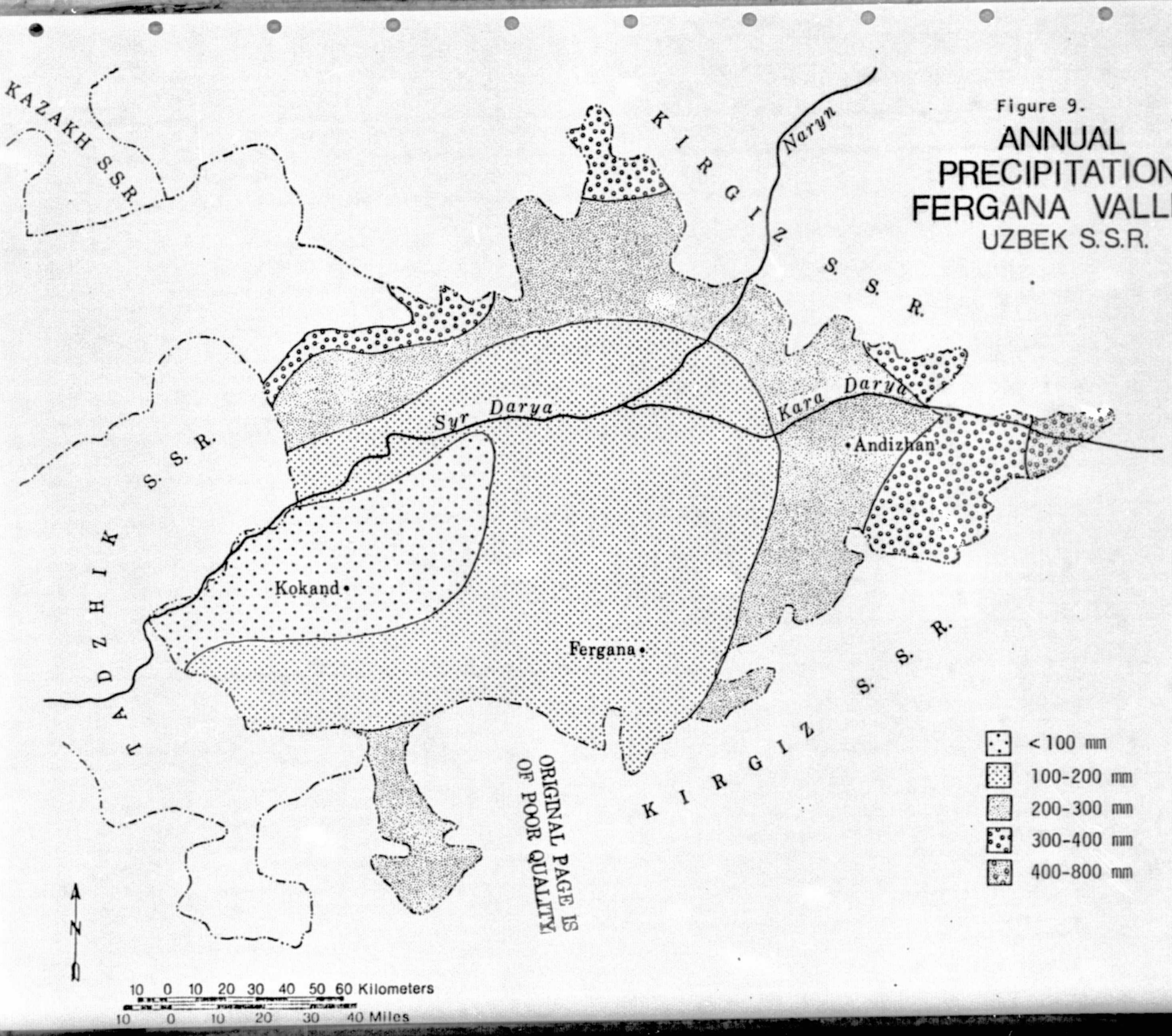

Figure 9.

ANNUAL PRECIPITATION: FERGANA VALLEY UZBEK S.S.R.

Table 3

NAMANGAN, U.S.S.R.													
PE	0	2	27	72	126	168	180	152	91	46	13	2	879
P	24	13	30	21	21	8	7	1	4	20	17	21	187
ST	52	63	66	56	39	23	13	8	6	5	9	28	
AE	0	2	27	31	38	24	17	6	6	21	13	2	187
D	0	0	0	41	88	144	163	146	85	25	0	0	692
S	0	0	0	0	0	0	0	0	0	0	0	0	0
FERGHANA, U.S.S.R.													
PE	0	0	20	67	116	164	184	153	92	38	9	0	843
P	22	14	26	19	21	11	6	3	2	14	17	16	171
ST	52	66	72	61	44	27	15	9	7	6	14	30	
AE	0	0	20	30	38	28	18	9	4	15	9	0	171
D	0	0	0	37	78	136	166	144	88	23	0	0	672
S	0	0	0	0	0	0	0	0	0	0	0	0	0
ANDIJAN, U.S.S.R.													
PE	0	1	22	99	120	159	169	140	88	38	13	1	850
P	27	22	38	24	22	10	6	2	3	19	17	20	210
ST	58	79	95	74	53	32	19	12	9	8	12	31	
AE	0	1	22	45	43	31	19	9	6	20	13	1	210
D	0	0	0	54	77	128	150	131	82	18	0	0	640
S	0	0	0	0	0	0	0	0	0	0	0	0	0
TASHKENT, U.S.S.R.													
PE	0	2	21	61	115	160	180	150	86	42	14	2	833
P	45	37	63	51	29	12	3	1	5	26	34	42	348
ST	127	162	204	197	148	90	50	30	23	22	42	82	
AE	0	2	21	58	78	70	43	21	12	27	14	2	348
D	0	0	0	3	37	90	137	129	74	15	0	0	485
S	0	0	0	0	0	0	0	0	0	0	0	0	0

PE Potential evapotranspiration
P Precipitation
ST Soil moisture storage
AE Actual evapotranspiration
D Water deficit
S Water surplus

(from Average Climatic Water Balance Data of the Continents, 1963)

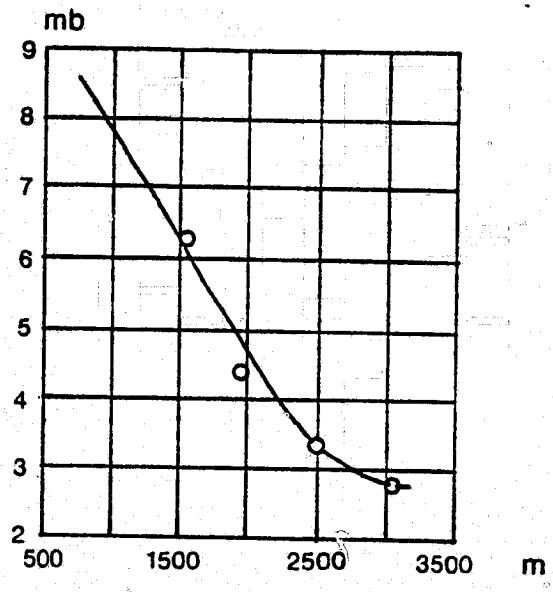

Figure 10. Variation of vapor pressure (mb) with elevation (m)

Soils

Soils of the Fergana Valley have widely varying water-physical properties. The semi-arid conditions that predominate in the region, in conjunction with topography and parent material, have produced a gray soil known as Sierozem. Sierozem soils develop under arid conditions on windblown deposits (loess), along piedmont areas, and on alluvial fans where rivers emerge from mountains. Sierozem soils cover only 2% of the USSR, but dominate the Fergana Valley (Figure 11). Small areas of soils such as Regosols and Lithosols can be found intermittently in the valley.

In the foothills to 1600 m elevation, sierozems develop beneath a grassy cover with ephemers (Figure 11). The sierozems have a scaly-laminated structure in the surface layer, changing into a slightly cloddy layer. Below lies a weakly compacted horizon with segregation of grains and concretions of carbonates, underlain by a layer rich in carbonates and gypsum. Biogenic constitution (foraminatedness and vesicularity) is distinctly evident in the sierozems of different kinds. The carbonate profile is well-defined, even though the entire soil is carbonate in character. The content of non-silicaceous salts is high, from 5 to 20 percent or more of the total soil mass. The sierozems differ in content of elements with water-resistant microstructure, that is, structural entities larger than 1.0 mm. But on the other hand, the water-resistant microstructure is well-defined: in fact, it is determined by the fairly favorable water-air properties - good water permeability and high, mainly capillary, porosity. The humus content in sierozems fluctuates from 1 to 4 percent. The specific weight of sierozems is 2.5 - 2.8; the bulk weight is 1.0 - 1.6; and the porosity is 50-60 percent. The total water permeability of the sierozems is 0.5 - 2.1 mm/min. (Resources of Surface Waters of the USSR, 1969)

Characteristic of the sierozems is a nonleaching type of water regime. The soil layers begin to be wetted in autumn or winter. Total wetting depth varies from 1 to 2 m. Sierozems in the western Tien-Shan in a 2 m layer have a water reserve of 382 mm (Karpov, 1960). At the end of March or the beginning of April vegetation starts rapidly drying up. Dessication is usually completed by May (Bode, 1963).

Using classification schemes developed in the US, Sierozem soils can be classified under the order of Aridisols or Xerosols. The classification Aridisol is from the Comprehensive Soil Survey System and Xerosol from the FAO-UNESCO soil map and "Soil System of the World" (Brady, 1974).

Aridisols are mineral soils found in arid climates. Except where there is ground water or irrigation, as is the case in much of the Fergana Valley, all of the soil horizons

are dry more than 6 months of the year. Consequently, they have not been subject to intensive leaching. They have an ochric epipedion generally light in color, low in organic matter, and may be hard and massive when dry. They may have a horizon of accumulation of calcium carbonate (calcic), often with an underlying layer of gypsum, or even more soluble salts (Brady, 1974). The Sierozem soils of the Fergana Valley come under the suborder Orthids. This suborder is broken down into two groups. The first group is composed of soils of gently or moderately sloping terrain, used mostly as range land with some irrigated crops. Areas in the United States that have similar soils include northeast Arizona, central and northeast New Mexico, southeast Colorado, and south-central Idaho. The second group includes soils of gently sloping to steep terrain. An area in the US that has a similar soil is north-central Nevada. Orthids are differentiated from other suborders of Aridosols by the absence of a horizon of clay accumulation.

Xerosol, another term used for the classification of desert or semi-desert soils is broken into four suborders, only three of which apply to soil types found in the Fergana Valley. They are haplid (typical xerosols or semi-desert soils), calcic (semi-desert soils with a distinct lime accumulaton horizon), and gypsic (semi-desert soils with a distinct gypsum accumulation horizon).

Sierozems are typically rich in calcium and form good agricultural soils when irrigated and fertilized. Without irrigation, Sierozems are not suitable for growing crops. Areas that are not irrigated are used for sheep and cattle grazing, but productivity per unit area is low.

Brown and chestnut soils are found at higher elevations. These soils develop under sheep's fescue and quack grass-motley grass-brush steppes, and can be found to an elevation of 3200 m. Loose loess and loesslike rocks on deluvial and eluvial deposits are the soil-forming rocks of this group. In mechanical composition they are fine-grained, rubbly, and rubbly-gravely. Humus content varies from 4 to 20 percent. The structure of the humus horizons is highly water-resistant and water-permeable, nutlike, or cloddy-granular, intergrading into coarse-cloddy with depth. The carbonate content in the upper part of the profile is 1 to 4 percent, and in the lower profile - to 10 percent. Physical properties of these soils may be described as follows: specific weight 2.5 - 2.8; bulk weight 0.6 - 1.1; and porosity 56 - 66 percent. The water permeability is 1.8 - 2.1 mm/min (Resources of Surface Waters of the USSR, 1969).

Light-brown meadow-steppe soils occupy the highest sections of the slopes of the ranges and their watersheds, reaching the perpetual snows. The soils are thin, contain from 3 to 20 percent humus, are weakly differentiated by horizons, and are rubbly. Soils underlie subalpine and

alpine compact meadow-steppe grass stands on deluvial and eluvial Paleozoic and moraine deposits. Sodding of the upper horizon and good granular structure is typical. The total porosity is 45 - 63 percent; porosity in the humus horizon is 57 - 60 percent.

Precipitation exceeds evaporation in the zone of meadow-steppe soils; this ensures a leaching type of water regime. Most of the zone is characterized by near-surface bedding of soil-groundwater; its surface rises into the soil profile during snow melt, during the spring-autumn rains, and sometimes even in heavy summer rains.

In the Padshaata River basin the light-brown meadow-steppe high-mountain soils (coarsely skeletal) are developed; they form amidst outcroppings of bedrock and in the region of glaciers and firns beneath sparse meadow vegetation, and are to be found in small isolated patches. The soil body is continuously wetted.

Principal soils in the Soviet study area are listed in Table 1.

A major problem in the agricultural areas of the test site is soil salinity. In areas of prolonged cultivation, such as the Fergana, excessive salts may accumulate. This is especially true of the central portion of the valley. These soils require careful drainage and salinty control. The soils near the perimeter of the valley, including the foothills and lower slopes of the mountains, are reasonably uniform in physical and chemical composition and do not contain harmful salts (Allworth, 1967, Burikin, 1967).

In the central and western parts of the valley there are sands and alkaline marshes. At the bases of the mountain ranges, broad fans of proluvial and deluvial gravel deposits occur (Suslov, 1961). Soils in these areas are not of much agricultural importance. They fall under the great soil groups of Regosols and Lithosols. Regosols are weakly developed soils on loose, non-alluvial deposits (loess, sand). The three suborders that apply are Eutric Regosols, Calcaric Regosols, and Dystric Regosols. Lithosols are non-arable soils, not even fit for grazing under most conditions. They are primitive, rubbly soils no more than 30 cm deep on bed rock (Brady, 1974).

Suslov, writing on the central desert portion of the valley states: "Intensive processes of weathering of Tertiary conglomerate and sandstone, and also of recent sandy alluvial deposits along the Syr Darya, lead to the creation of considerable areas of shifting sand. Only along the margin of the valley is the sand somewhat secured by vegetation. The partially mobile sand of the center accumulates in recent barchans, with heights up to 50 feet, which move east, covering fields and settlements."

Writing about the gravel deposits, Suslov makes note that the gradual erosional "disintegration of these formations creates, at first, individual table mountains, and, later, a highly broken relief. The rivers have large dry deltas, as for example, the huge alluvial fan of the Sokh River, which irrigates Kokand Oasis, and the delta of the Isfayram River."

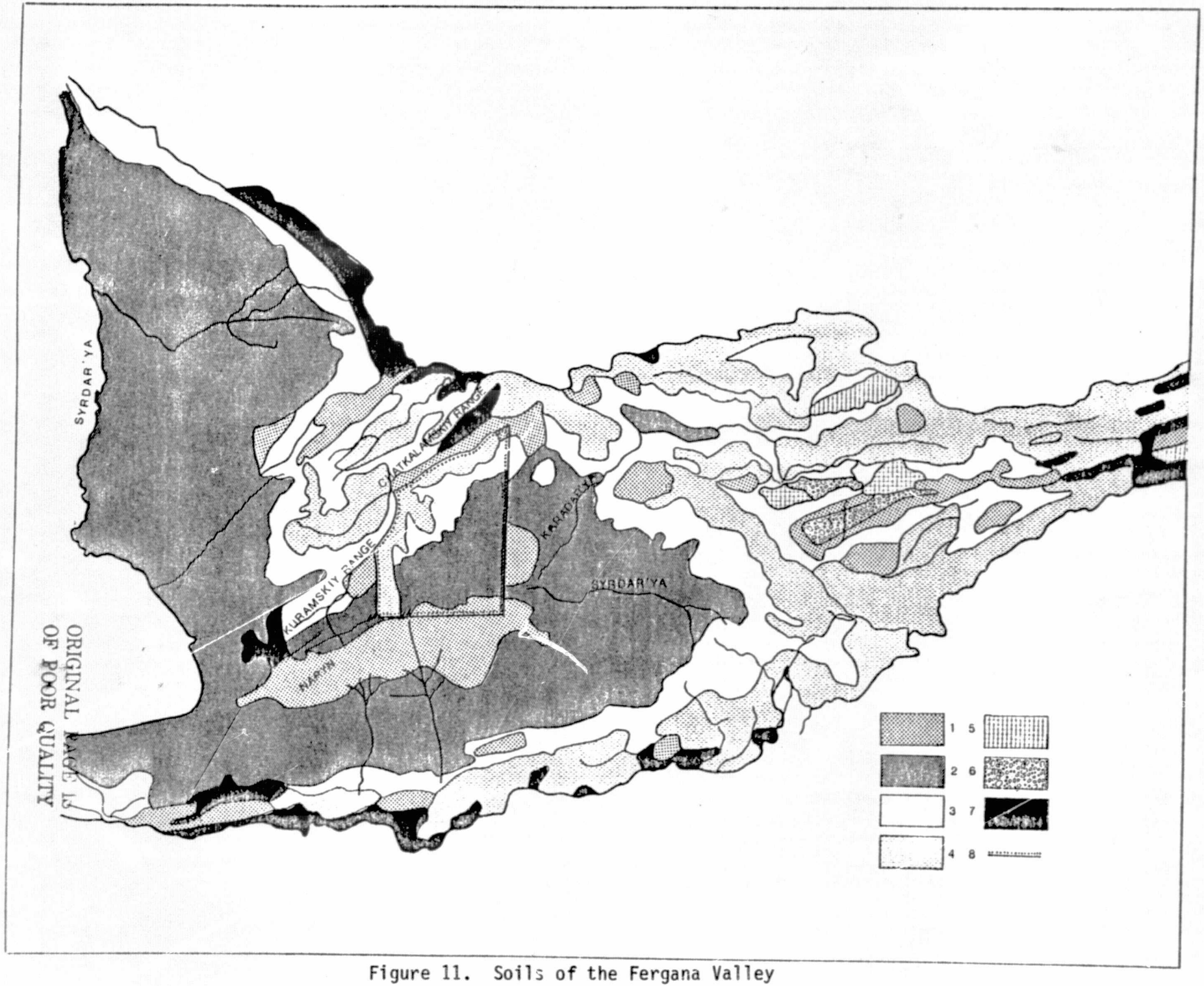

Figure 11. Soils of the Fergana Valley

Completion of caption to Figure 11 on preceding page

1. gray-brown desert, takyr, and sandy soils of the plains
2. zone of sierozems, mountains and foothills
3. zone of dark brown and chestnut soils
4. zone of light-brown soils of high-mountain steppes
5. high-mountain and desert-steppe takyrlike and syrt soils
6. strongly salinated soils on salt-bearing Tertairy deposits
7. light-brown, meadow-steppe, high-mountain soils, eroded, coarsely skeletal amidst outcroppings of bedrock, firns, and glaciers
8. boundary of region

Geology

The Fergana Valley lies on the north western edge of the Pamir Range, the highest mountain range in the USSR. The Pamirs were uplifted when the Indian plate collided with the Asian plate during the Cenozoic (Dietz and Holden, 1970). Tectonic activity from plate movements during the Quaternary created the Fergana Valley and the mountain ranges which surround it (Figure 12). The Fergana is a drop block valley surrounded by rapidly uplifting mountain ranges (Belousov and Gzovskii, 1958). The area is described by the Ministry of Geology, USSR, as a region of perigeosynclinal complexes which are part of the tectonic regime of the Scythe-Turanian structures (Ministry of Geology, 1964). Figure 13 is a stylized map of the Fergana area showing the general tectonic structure and seismic activity.

The Fergana geosynclinal region can be divided into mountain and foothill sections. The study area includes diverse topography - from alpine zones through regions of medium- and low-elevation, to foothills and flatland. The average elevations of the river watersheds in the study area vary from 2300-2800 m. Regions of medium-elevation relief are dissected by deep and narrow valleys, while regions of low-elevation contain numerous valleys, gorges, ravines and kettleholes.

The geologic structure of the study area and its surroundings are associated somewhat with the terrain. There is a consistent shift from the periphery to the crests of the ranges of geologic blocks which differ in age, composition, degree of dislocation and hydrologic characteristics. Older, consolidated igneous and metamorphic rocks are found at higher elevations while less consolidated Quaternary deposits are found at the foot of slopes, along the floors of valleys, and in karst basins. The Kuramin and the southwest portion of the Chatkal ranges are composed chiefly of recent intrusive igneous rocks and older (Paleozoic) metamorphic rocks. Intrusive and extrusive igneous rocks contain fissures more than 50 m deep and hence form good water reservoirs. Clayey and sandy slates, also widespread, are nearly impermeable. Fissures contained within them are usually narrow and shallow in depth (to 30 m), so their water storage capacity is also small and few springs issue from these rocks. Pure limestones are rarely found in the area. In places, deluvial formations overlie the broken terrain of the mountain ranges. The foothills and valley floor are composed of Tertiary sediments and Quarternary alluvium from the surrounding mountains. Lithologic complexes in the watersheds are shown in Table 1.

The Fergana Valley is seismically active. A major fault runs along the north side of the valley at the base of the Kuramin, Chatkal and Fergana Mountain Ranges. Faulting is evident on all sides of the valley from geophysical evidence and geothermal activity (Ministry of Geology, 1966E; Baranov, 1969).

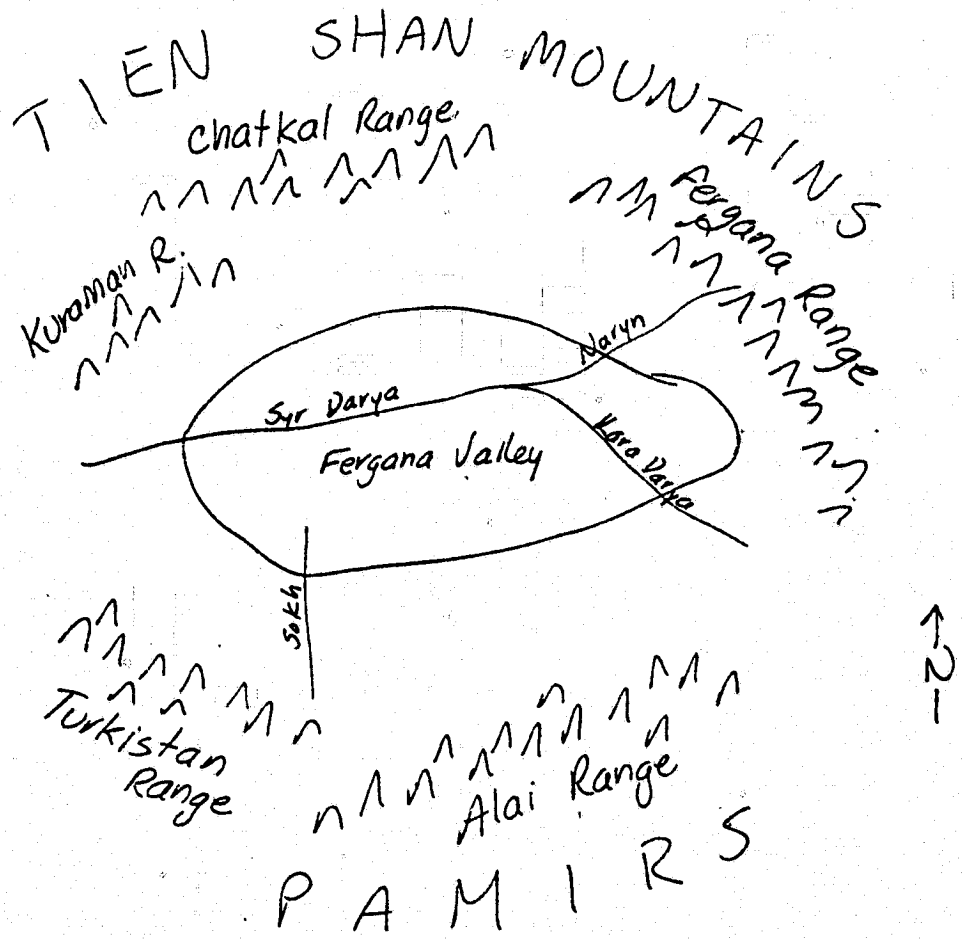

Figure 12. Fergana Valley and surrounding mountain ranges.

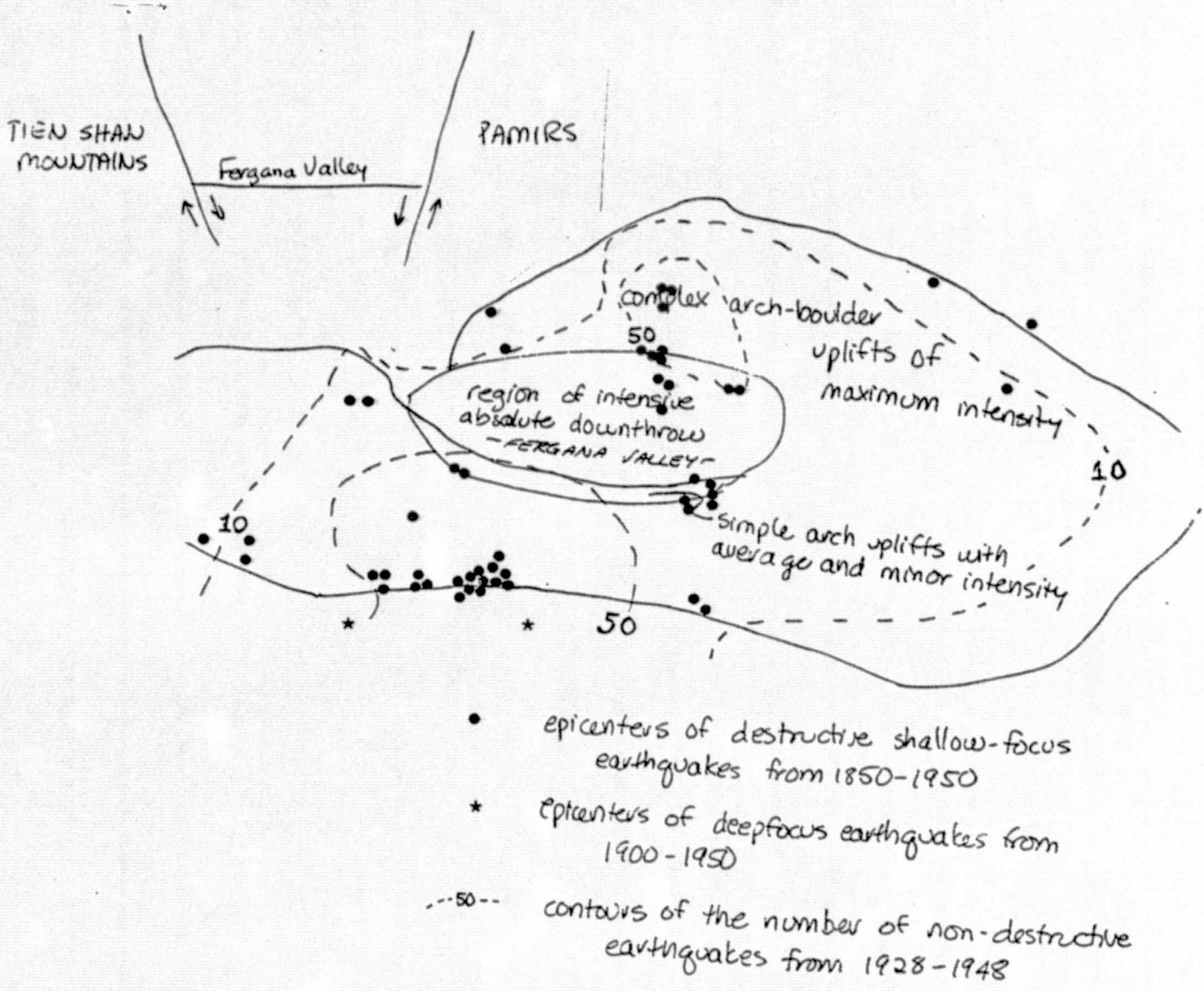

Figure 13. General tectonic structure and seismic activity of the Fergana Valley region (after Belousov and Gzovskii, 1958).

Hydrogeology

Groundwater conditions in the Fergana Valley are the result of varying aquifer-system characteristics such as aquifer materials, altitude, locational relation to irrigation outflow points, and location in relation to other water-bearing or water-confining rocks. The hydrogeology of the study area is determined largely by the structural geology. Due to the varying water-bearing nature of the different rocks and unconsolidated deposits and their subsurface spatial variation, the groundwater characteristics vary spatially even within a given water body (Figure 14).

Infiltration in the mountainous areas supplies groundwater to the Fergana basin. There is however little surface water infiltration at the higher elevations in the zone of igneous and metamorphic rocks. Infiltration mainly occurs from channels which flow through the less consolidated late Tertiary and Quaternary fluvial, alluvial and glacial deposits. Most infiltration replenishes groundwater; some re-emerges in depressions both at springs and rivers, and some supplies flows in the alluvial fans of the streams. Groundwater in the study area is supplied primarily by infiltration from surface streams. Carbonate bedrock provides a supplementary source of groundwater. Atmospheric precipitation typically plays a small part in supplying the groundwater, since the water table lies at considerable depth. The denudation of the mountain ranges and the large local slopes provide good drainage and favorable conditions for intensive water turnover. Because of the slopes in the Zaadyr and Mezhadyr depressions, groups of groundwater flows, supplied by infiltraton from numerous surface streams, are formed in this part of the study area.

The aquifer system of the area may be broken down to include three categories: 1) shallow water body, 2) unconfined and semi-confined water body and 3) confined water body. A shallow water body is defined as groundwater that occurs at shallow depth in shallow wells (this may be a perched water body) that is usually semi-discrete from other groundwater bodies. Shallow water bodies are commonly supported by a relatively impermeable layer of fine sediments, silts or clay. These bodies occur only in younger alluvium and probably in the flood basin deposits where water bearing deposits are interlayered with lacustrine and marsh sediments. These water bodies often result in salinity problems and mainly occur in the bottom of the Fergana Basin in areas of marsh and solonchak (or developing horizons), and are common in the Adyr area of alluvial terraces (Suslov, 1961).

Unconfined water bodies may be identified from well data as having little or no difference in head with varying depth. These usually occur in unconsolidated deposits that

are not interbedded with fine grained lacustrine or marsh deposits. Tertiary conglomerate and sandstone overlain in the foothills by broad fans of proluvial and deluvial gravel deposits such as in the desert pastures on the margin of the Fergana Basin are conducive to such environments. The unconfined groundwater bodies found in the Zaadyr and Mezhadyr depressions of the study area have no pressure head and lie in boulder-gravel deposits at considerable depth.

Semi-confined and confined conditions occur where the water body is bounded at the base and/or surface by impermeable layers of soil, regolith, or rock. These water bodies tend to occur in lower valley areas adjacent to foothill terraces and in the central portion where alluvial materials, loess, and varying-facie fluvial material are interbedded and interfingering. In the Soviet study area, they occur along the periphery of the Zaadyr and Mezhadyr depressions where water-bearing horizons are enclosed between relatively impermeable clay formations. A pressure head is created by the slope gradient from the low foothills (adyr) along the borders of the depresssions. When these horizons contact sandy gravel deposits, numerous springs occur.

Groundwater of the Northern Fergana depressions (Kassansay, Gavasay and other river basins) is found mainly in alluvial and proluvial gravel deposits. In the north, close to the foothills of the adyr, the gravel beds are exposed; in the south they are overlaid by sandy loams and loams, creating confined aquifer conditions. The thickness of the loam deposits varies from 2-3 m in the north to 20 m or more at the Syr Darya. The alluvial fans of the rivers in the study area are incompletely manifested, since the rivers have swept away their peripheral parts. Within each alluvial fan there is a specific zone of ground and sub-head water flow.

The alluvial fan of the Kassansay River, south of the Kassansay and Namanganskiy adyr, is 11-12 km wide and 20-25 km long. Its southern limit is found between the first and second terraces above the floodplain of the Syr Darya. Here the flow of groundwater is supplied mainly by infiltration from the Kassansayskaya trans-adyr and the Kukumbayskaya mezh-adyr depressions. It is additionally recharged by infiltration from surface streams, which form a complex hydrographic network on the alluvial fan. In the upper part of the fan, the water table lies at a depth of 40-60 m; this depth decreases as the flow approaches the Syr Darya.

Water also flows along faults or through the karst regions of carbonate rocks. Water along faults (bordering the valley) in addition to the underflow discharge from mountain slopes and valleys raises the level of water bodies in the three categories discussed above and leads to the salinizing and swamping of lowlands (Suslov, 1961). Jointed metamorphic and igneous rocks have structurally controlled

water permeability. They are overlain by shales, with interbeds of sandstone. Groundwater in these rocks is less abundant than in the limestones and is characterized by low mineral content, monclithic aquifers, and less fissuring to provide storage.

Mineralization of the groundwater confined in Mesozoic and Cenozoic formations gradually increases with distance from the point of recharge. However, the mineral content of water emerging at springs does not exceed .5 g/liter; the water type is calcium hydrocarbonate and calcium-magnesium hydrocarbonate.

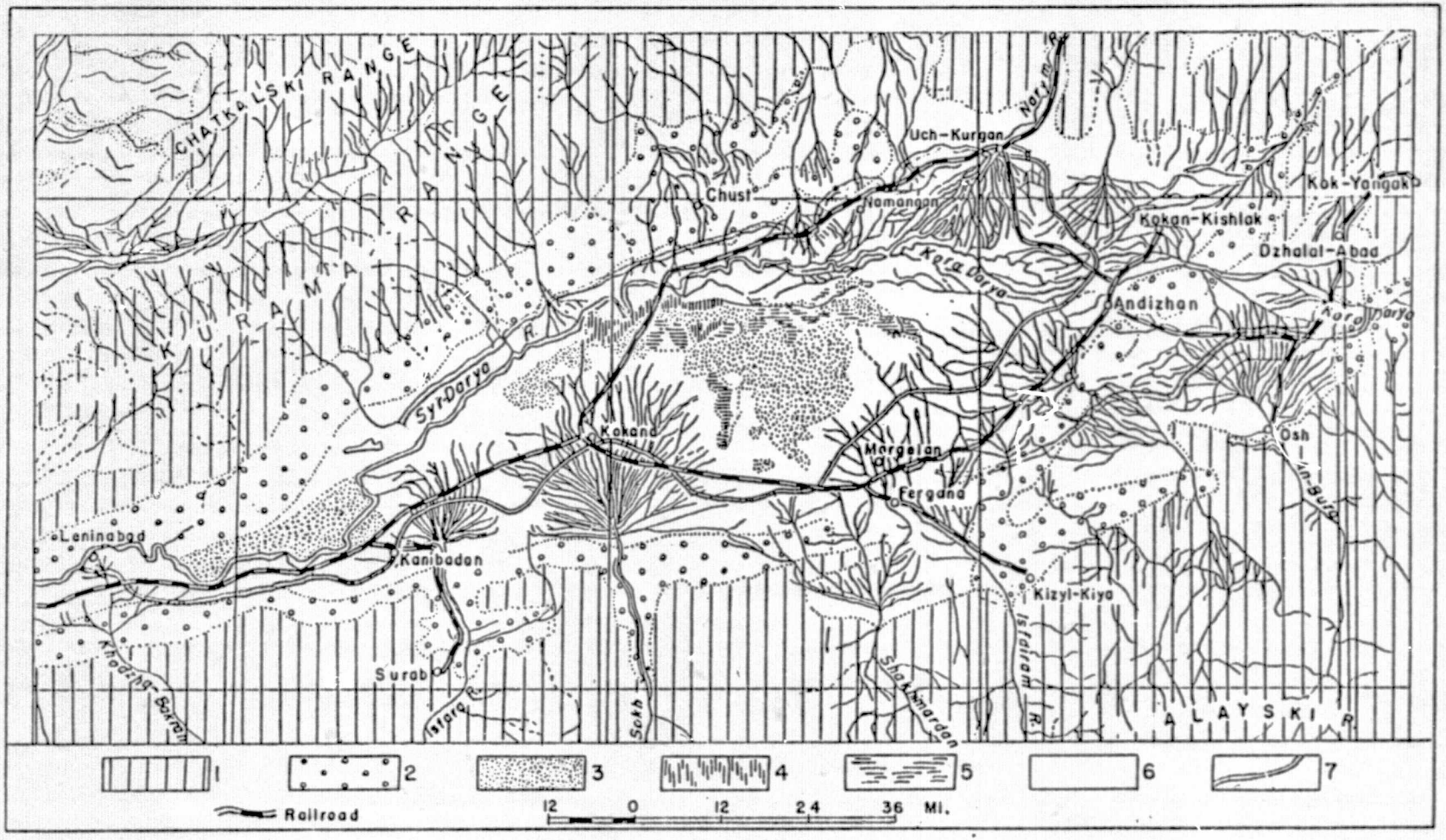

Figure 14. Geomorphological scheme of the Fergana Valley: 1 - Mountains surrounding the valley; 2 - Adyr area of alluvial terraces; 3 - Moving and fixed sand; 4 - Solonchak; 5 - Marsh; 6 - Cultivated oases; 7 - Fergana Canal (from Suslov, 1961).

Snow Hydrology

Precipitation falls as snow mainly from November through March. On the southern slopes of the Chatkal Range, from 25 to 45 days with snow are observed at the 1000-1500 m elevations.

Snow depth and the water content of the snowpack vary. In the middle elevation zone, snow depth is typically 80-90 cm, though in some years it reaches 100-110 cm. On the southeastern slopes of the Chatkal Range, at elevations from 1400 to 2200 m, the water content of the pack varies from 100 to 225 mm. In some years in the Padshaata River basin it reaches more than 375 mm. Figure 15 shows the distribution of water content of snow cover by elevation in the Gavasay River in 1942.

Dates of ablation vary with elevation. In the foothills, at elevations to 1500 m, the snow cover typically forms during the second and third ten-day periods in November and disappears during the second and third ten-day periods of March. At elevations of 1500-2500 m, snow cover forms at the end of October and persists till the end of April. At elevations above 3000 m; snow covers the ground from the second ten-day period of September until the first ten-day period of June.

Streams in the Syr Darya basin are primarily supplied by meltwater. The indicator of the river recharging type was calculated as the ratio of the discharge in July to September to the discharge in March to June. Using this method, the rivers in this region can be classified as rivers whose annual discharge is determined mainly by fluctuations in precipitation. The effective precipitation in the area is retained in storage as snow and released as snow melt periodically to the basin's channels (the major ones being the Syr Darya, Naryn, and Kara Darya Rivers). The Syr Darya and Naryn have mixed glacial-snow feeding resulting in two high water periods: in spring (April-May) from melting snow, and in summer (June-July) during the period of ice thaw (Suslov, 1961). Their tributaries are supplied primarily by snowmelt in the spring. In April these rivers manifest violent activity, yet by July an abrupt reduction of discharge is observed due to depletion of seasonal snow cover. The variability of annual discharge in snow-fed streams is determined primarily by the variation in the water content of snow at the beginning of snowmelt. The variability in meltwater from perpetual snows and glaciers, on the other hand, is not dependent on the amount of annual precipitation, but is determined largely by the amount of energy received by the surface of the snow and ice. (Tables 4 and 5)

Because meltwater is the main source of river recharge, the distribution of discharge through the year is determined mainly by the accumulation of snow and ice in the mountains,

and partly on variability in infiltration and evaporation. Not only the amplitude of fluctuations in the annual discharge, but also the long-term trend of discharges from Central Asia streams are determined by their supply source - meltwater from seasonal snow and/or from perpetual snows and glaciers. All the streams in the Fergana Valley are classified as snow-glacier and snow-fed streams. In the mountain regions the amount of precipitation generally increases with elevation, while vapor pressure decreases with increased elevation and lower temperatures (Figure 10). For this reason the discharge norm typically increases with elevation. However, since the amount of precipitation and discharge in the mountains is also influenced by the orientation of the slopes in relation to the prevailing direction of the movement of air masses, the dependence of discharge on elevation shows up most clearly for relatively restricted orchydrographic regions.

Table 6 shows the distributuion of snow surveys in the study area.

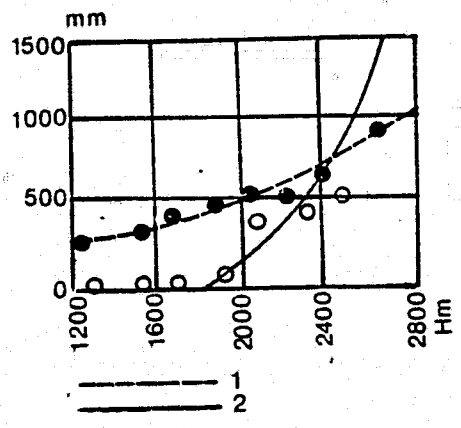

Figure 15. Variation of water content of snow cover with altitude. (Basin of Gavasay River, 1942)

1 = water content at end of February

2 = water content at end of March

RIVER-POST	ADOPTED CALCULATED PERIOD OF OBSERVATIONS OF DISCHARGE, YEARS	δ	r_{tx}	r_{yt}	r_{yx}	C_v, ANNUAL DISCHARGE IN CALCULATED PERIOD	METEOROLOGICAL STATIONS FROM WHICH METEOROLOGICAL FACTORS ARE RECORDED	ELEVATION OF METEOROLOGICAL STATION, m
Gavasay River, Mouth of the Ters River	1937-60	0.26	-.37	0.33	0.80	0.28	mouth of the Ters River	1818
Padshaata-Mouth of the Tostu River, 2.6 km above Mouth	1936-60	0.66	-.48	-.45	0.68	0.21	mouth of the Tostu River	1529

Table 4. Coefficient of Correlation between Discharge of Water and Meteorological Factors (Precipitation and Above-Zero Air Temperatures)

BASIN	OBSERVATIONS	ELEVATION	NUMBER OF		
			Snow-Stations	Precipitation Meters	Airborne-Controlled Staffs
Gavasay	1927	1200-2700 m	23	3	9
Padshaata	1928	1360-2190 m	19	2	-

Table 6. Snow Surveys

RIVER	STATION	AREA OF WATERSHED km^2	MEAN ELEVATION OF WATERSHED	OBSERVATION PERIOD	TOTAL NUMBER OF YEARS OBSERVED USED IN STUDY	MEAN DURING OBSERVATION PERIOD			MEAN DURING MULTIANNUAL PERIOD			CALCULATED VALUE OF C_v	ADOPTED VALUE C_v
						Velocity of Water Flow m^3/sec	Modulus of Discharge liters/sec per km^2	Layer of Discharge mm	Velocity of Water Flow m^3/sec	Modulus of Discharge liters/sec per km^2	Layer of Discharge mm		
1	2	3	4	5	6	7	8	9	10	11	12	13	14
Padshaata	Mouth of Tosto River	366	2830	1925-62	37	6.01	16.4	517	6.03	16.7	526	0.20	0.21
Chanach	Chanachsay	133	2630	1938, 1941, 1944, 1949, 1950, 1952, 1955, 1956, 1959-62	12	(1.76)	(13.2)	(416)	(1.76)	(13.2)	(416)	--	--
Kassansay	Mouth of the Uryukty	1240	2480	1945-62	18	8.93	7.20	227	(8.50)	(6.85)	(216)	0.26	--
		1780	2330	1925-42	16	9.80	5.50	173	(10.8)	(6.07)	(191)	0.27	0.30
	River, Baymak kishlak	1780	2330	1925-60 1962	35	10.8	6.07	191	10.8	6.07	191	0.28	--
Uryukty	Uryuktysay	86.5	2180	1941, 1947, 1948, 1950, 1960, 1962	7	(0.64)	(7.40)	(233)	(0.62)	(7.17)	(226)	--	--
Uryukty	Mouth of Uryuktysay River	116	2190	1947-62	16	0.48	4.14	130	(0.45)	(3.88)	(122)	0.37	--
Alabuka	Alabukasay	208	2520	1938, 1941, 1944, 1952, 1955, 1957-62	18	(2.53)	(12.2)	(383)	(2.40)	(11.5)	(363)	--	--
Sumsar	Sumsarsay	90.0	2600	1941, 1945-50, 1959	8	(1.01)	(11.2)	(353)	(1.00)	(11.1)	(350)	--	--
Koksarek	Koksareksay	96.2	2510	1941	1	(0.78)	(8.11)	(255)	(0.90)	(9.36)	(295)	--	--
Gavasay	Mouth of the Beshtashata River	288	2840	1932-38	6	(3.82)	13.3	419	(4.20)	(14.6)	(460)	--	--
Gavasay	Mouth of the Ters River	361	2840	1932-62	31	4.96	13.7	432	5.05	14.0	441	0.28	0.28
Gavasay	Gava kishlak	657	2460	1925-62	36	5.98	9.10	287	6.29	9.57	301	0.31	0.32

Table 5. Discharge of Rivers in Test Area

1	2	3	4	5	6	7	8	9	10	11	12	13	14
Ters	Besh-Tash winter camp	30,3	2860	1932-37	--	--	--	--	(0,52)	(17,2)	(540)	--	--
Beshtashka	Mouth	36.6	2710	1932-37	--	--	--	--	(0,18)	(4,92)	(155)	--	--

Table 5 (continued). Discharge of Rivers in Test Area

General Hydrology

Streams in the study area are also supplied, to some extent by inflow of groundwater from mountain valleys and slopes. This source is also indirectly dependent on snowmelt, since groundwater recharge is determined primarily by the volume of meltwater. Streams fed from groundwater occur in the upper foothill belt (up to 1000 m) and are fed by groundwater and showers. They tend to have small steady or intermittent discharges with occasional flash flooding during intense storms (Suslov, 1961).

The Syr Darya follows the northern rim of the Fergana Valley. Its upper section, the Naryn River, enters the valley from the east through the Fergana Range. Surface water in the basin occurs as flow in the Syr Darya, in its tributaries (including the Sokh River), in the dense network of irrigation, and as standing water in shallow closed basins and artificial reservoirs (Figure 2).

In the study area, the Gavasay, Sumsar, Kassansay and Padshaata rivers have the highest discharge of streams which drain the southeastern slopes of the Chatkal range and the Kuramin mountains. All these rivers are right bank tributaries of the Syr Darya. These rivers do not freeze over widely, (the period when these streams are frozen typically does not last longer than 80-90 days), however, local freezing can lead to the formation of major ice jams which create significant fluctuations in water level during their formation and breakup. Formation of floating ice is promoted by high flow velocities, rocky, rapids-filled water, etc. These ice formations can last two or even three months.

The turbidity of water in the Chatkal Range varies from less than 0.1 kg/m^3 to 0.3 kg/m^3. In spring and the first half of summer, all rivers draining these mountains carry mudflows, often with destructive force.

Figure 16 shows that, at the same elevations, the Padshaata River basin is characterized by greater discharge moduli than the basins of the Gavasay and Kassansay Rivers. At the elevation of 1600 m the discharge modulus of the Padshaata River is 1.0 liter/sec km^2, while in the Gavasay and Kassansay rivers it is 0.5 liters/sec km^2. This is due to the areal distribution of precipitation, which varies with the orientation of the basins. The discharge of the Gavasay and Kassansay rivers, whose valleys are unfavorably oriented, averages 8 liters/sec km^2. Further to the east, orientation is more favorable, so the moduli of the discharge of the Padshaata River and several left bank tributaries of the Kassansay River increase to about 11 liters/sec km^2.

The period of greatest discharge from streams in the study area occurs from March to August or September. 75-85% of the annual discharge occurs at this time. The highest

annual flow velocities typically occur in May; however, the discharge of the Padshaata River is highest in June. Low water lasts from September to March. Coefficients of variation, describing the annual distributuion of flow, are shown in Table 7. Table 8 shows the monthly distributuion of discharge as a percent of annual discharge. The relatively low elevations of the Chatkal and Kuramin Ranges account for the similarity in the discharge of the streams in the study area. Generally, then, three periods can be distinguished:

1. The period of snow high water, formed mostly by the meltwater from seasonal snows at low to mid-elevations. The onset of this high-water period is associated with the onset of stable, above-zero temperatures. The volume of discharge is determined by the amount of snowfall of the given year. This period typically lasts from March-June.

2. The period of snow-glacier high water, formed mainly by the meltwater from high-mountain snows and glaciers. This period coincides with the hottest part of the year (July-September).

3. The period of low-water, when the streams are supplied primarily by groundwater. This period is characterized by stable, relatively low discharge and by the absence of diurnal fluctuations. It typically lasts from October-February.

The characteristics of high-water and low-water periods of the rivers in this region, and the maximum and minimum volume flows are in Tables 9, 10 and 11. Table 12 shows the types of measurements taken at the hydrometeorological stations in the study area.

Movement of surface water and groundwater in the Fergana Basin may be described by an inflow-outflow budget accounting for the different modes of water transport. The primary inflow components (precipitation, streamflow and groundwater) have been described above. The total water resources of the entire Syr Darya basin in 1968 were estimated to be about 35 sq km (Kritskiy, 1968). About two-thirds of the arriving runoff is expended on irrigation of fields, evaporation from the river channels and reservoirs, and the periodic flooding of lowlands. Water loss also occurs by infiltration (underflow or throughflow) evaporation from surface water and evapotranspiration. The remaining discharge flows to the Aral Sea.

The main inflow components of the Fergana Basin may then be summarized as: 1) river flow from the Kara Darya and Naryn, 2) stream and river flow from the surrounding mountains (Tien Shan, Pamir-Alai), 3) effective precipitation in the form of snow and ice melt, and 4) underflow or throughflow of groundwater from the mountains. The main outflow components include: 1) discharge of the Syr

Darya surface waters out of the Fergana Basin, 2) infiltration or underflow losses of groundwater out of the basin, 3) evaporation from standing and flowing surface water, and 4) agricultural and vegetation losses (evapotranspiration).

Careful management of water resources in the Fergana Basin is required to maximize the resource benefits. An increase in consumption of water can promote conditions in which irrigation needs are not met. This is shown by the fact that the water level in the rivers does not always ensure the entry of the water at the heads of the irrigation systems. A considerable portion of the runoff in the area passes in the form of high, brief high-water peaks superimposed on the meltwater wave. On rivers which are fed by runoff from relatively low mountains or small drainage basins, much water passes at the beginning of the warm season, prior to the basic irrigation period.

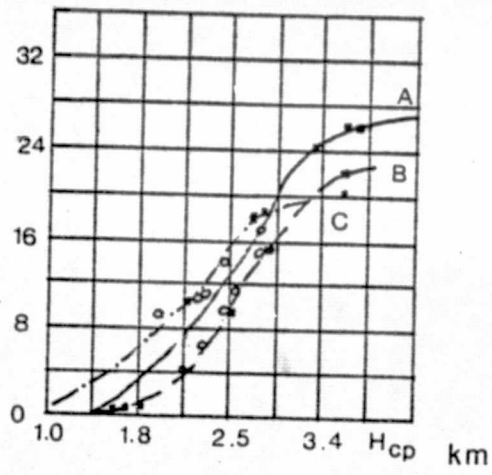

Figure 16. Dependence of modulus of discharge on mean elevation of watershed (km)

A. Padshaata River
B. Kassansay River
C. Gavasay River

RIVER, STATION	COEFFICIENT OF VARIATION OF SEASONAL DISCHARGE		
	Spring	Summer	Autumn-Winter
Padshaata, mouth of the Tostu River	0.23	0.27	0.22
Kassansay, Baymak kishlak	0.32	0.52	0.29
Gavasay, mouth of the Ters River	0.28	0.44	0.29
Gavasay, Gava Kishlak	0.35	0.44	0.26

Table 7.

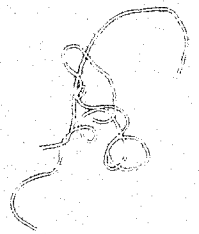

RIVER, STATION, WATER LEVEL OF YEAR	MONTHLY DISCHARGE											
	Jan	Feb	Mar	Apr	May	June	July	Aug	Sep	Oct	Nov	Dec
Padshaata, Mouth of the Tostu River												
High Water	2.4	2.1	2.7	8.7	17.0	21.9	17.8	10.5	5.8	4.1	3.8	3.2
Medium	3.3	2.9	3.1	7.8	17.8	21.8	16.8	10.2	6.0	4.0	3.6	2.8
Low Water	3.1	2.8	3.4	6.8	17.1	23.5	15.8	9.6	6.0	4.6	3.7	3.6
Very Low Water	3.3	2.9	3.4	6.8	17.3	23.7	15.1	9.2	5.7	4.8	4.0	3.8
Kassansay Baymak kishlak												
High Water	2.7	2.2	1.9	6.7	15.9	22.7	18.1	14.9	6.4	2.9	2.4	3.2
Medium	2.8	2.7	3.1	6.1	17.4	23.2	17.0	11.9	5.2	3.7	3.7	3.1
Low Water	3.0	2.7	4.0	9.0	16.9	22.1	14.5	8.6	5.6	5.3	5.0	3.3
Very Low Water	3.1	2.8	4.6	10.2	19.2	25.1	10.6	6.3	4.1	5.4	5.2	3.4
Gavasay, Mouth of the Ters River												
High Water	1.4	1.4	1.8	9.8	33.3	25.8	11.9	4.9	2.8	2.6	2.4	1.9
Medium	1.9	2.2	2.2	11.6	23.3	34.6	9.9	4.6	3.0	2.5	2.5	1.7
Low Water	1.9	1.7	3.3	9.6	35.9	23.5	8.2	4.3	3.1	3.2	2.8	2.5
Very Low Water	2.1	1.9	3.4	9.7	36.2	23.7	7.2	3.8	2.7	3.4	3.2	2.7

Table 8. Distributuion of Discharge (in percent of annual discharge)

RIVER, STATION, WATER LEVEL OF YEAR	MONTHLY DISCHARGE											
	Jan	Feb	Mar	Apr	May	June	July	Aug	Sep	Oct	Nov	Dec
Gavasay, Gava kishlak												
High Water	1.7	1.6	2.2	12.2	30.9	23.9	11.5	5.3	3.0	2.7	2.8	2.2
Medium	2.1	2.0	2.5	10.3	32.4	23.7	9.9	5.1	3.5	3.0	2.9	2.6
Low Water	2.5	2.3	3.6	8.8	32.8	23.5	8.9	4.4	3.4	3.5	3.4	2.9
Very Low Water	2.9	2.6	3.6	8.8	32.6	23.4	8.0	4.0	3.0	3.9	3.9	3.3
Chaadak (Chaadaksay), Mouth of the Dzhulaysay River,												
High Water	1.5	1.7	3.2	15.6	24.6	31.3	9.3	4.1	2.3	2.2	2.3	1.9
Medium	1.9	2.0	3.8	14.0	33.6	22.6	8.0	3.9	2.7	2.8	2.5	2.2
Low Water	2.3	2.7	4.8	11.9	36.6	20.3	6.8	3.4	2.8	2.9	3.0	2.5
Very Low Water	2.9	3.5	4.7	11.7	35.8	19.9	5.6	2.8	2.3	3.7	3.9	3.2

Table 8 (continued). Distribution of Discharge.

RIVER, STATION	PERIOD OF OBSERVATIONS		CHARACTERISTICS	DURING PERIOD OF OBSERVATION				
				Highest		Mean-Multiannual		
	Years	Number of Years		Q, m^3/sec; h, mm	Year	Q, m^3/sec; h, mm	Modulus of Discharge, liters/sec	C_v
Padshaata, Mouth of the Tostu River	1926-62	37	Q_{max}	44.5	1928	28.1	26.8	0.28
			Q_{mt}	--	--	22.5	61.4	0.27
			h	623	1960	408	--	0.24
Kassansay, Mouth of the Uryukty River	1952-62	11	Q_{max}	84.8	1953	51.6	41.6	0.30
			Q_{mt}	--	--	46.7	37.6	0.30
			h	161	1952	104	--	0.36
Kassansay, Baymak kishlak	1926-41	16	Q_{max}	132	1928	68.3	38.4	0.40
			Q_{mt}	--	--	--	--	--
			h	239	1934	132	--	0.36
Gavasay, Mouth of the Ters River	1933-62	30	Q_{max}	(55.7)	1934	38.0	105	0.23
			Q_{mt}	--	--	29.8	82.4	0.24
			h	601	1949	362	--	0.35

Table 9. Maximum Annual Velocities of Water Flow (Q_{max}, m^3/sec), Maximum Discharge Flow Rates of Meltwater (Q_{mt}, m^3/sec) and Discharge Layer (h, mm) in Freshet Period.

RIVER	STATION	AREA OF WATERSHED km^2	PERIOD OF OBSERVATIONS	NUMBER OF OBSERVATION YEARS	LOW-WATER PERIOD				
					Mean Date Beginning	Mean Date Ending	Duration, Days	Mean Consumption During Low Water Period m^3/sec	Layer of Discharge, mm
Padshaata	Mouth of the Totsu River, 2.6 km above mouth	366	1931-34 1936-48 1951-62	29	9/16	3/24	190	2.37	106
Gavasay	Mouth of the Ters River	361	1936,1937, 1939-62	26	8/16	3/24	221	1.40	74.0
Gavasay	Mouth of the Gava River	657	1936-62	27	8/31	3/27	209	1.86	51.1

Table 10. Characteristics of Low Water Period

RIVER	STATION	MEAN ELEVATION OF WATERSHED m	PERIOD OF OBSERVATIONS (ASSUMED)	NUMBER OF YEARS	MINIMUM DAILY DISCHARGE liters/sec km^2	MONTHLY MEANS FOR PERIOD OF OBSERVATION		COEFFICIENT OF VARIATION	COEFFICIENT OF ASYMMETRY
						Consumption of water m^3/sec	Modulus of Discharge Liters/sec km^2		
Padshaata	Mouth of the Tostu River, 2.6 km above the mouth	2830	1936-62	30	4.46	1.82	4.97	0.21	0.6
Gavasay	Mouth of the Ters River	2840	1937-65	29	1.88	0.92	2.55	0.31	1.0
Gavasay	Gava kishlak	2460	1936-66	31	1.45	1.37	2.08	0.24	0.6

Table 11. Mean Monthly and Diurnal Discharge.

RIVER STATION	DISTANCE FROM MOUTH, KM	AREA OF WATERSHED KM²	PERIOD OF OBSERVATION						MAXIMUM VELOCITIES OF WATER FLOW & LAYER OF FRESHET DISCHARGE	PRESENCE OF METEOROLOGICAL STATIONS (M/CT) AND POSTS (M/P)
			Level	Velocity	Temperature	Glaciation	Suspended Detritus	Chemical Composition		
1	2	3	4	5	6	7	8	9	10	11
Padshaata, mouth of the Tostu River, 2.6 km above mouth	92	366	1954-64	1934-70	1953-70	1936-69			1926-33 1935-48 1950-70	M/CT
Padshaata, Yangikurgan kishlak	42	--	--	1941-51 1953-62	--	--	--	--	--	--
Chanach, Chanachsay, 8 km from the village of Aktam	15	133	--	1938-41 44,49,50 52,55,56 59,68,70	--	--	--	--	--	--
Kassansay, Kyzyl-Tokay kishlak	74	1130	--	1967-70	--	1967-70	1968-70	1968-70	1967-70	--
Kassansay, mouth of the Uryukty River	66	1240	1951-67	1945-68	1952-68	1951-68	1956-68	1962-68	1951-68	--
Kassansay, Uryukty River	59	1430	1957-70	1957-70	1957-70	1957-70	--	--	--	--
Kassansay, Baymak kishlak	52	1780	1925-42	1925-60 1962	--	--	--	1938	--	--
Kassansay, Gergeuchi kishlak	34	--	--	1953-59	--	--	--	--	--	--
Kassansay-Kuyuk Madarskiy at the head of the Akhsokay Channel	23	--	--	1932-44 1947-52 1960,62	--	--	--	--	--	--
Uryukty-Uryuksay, 8 km north of the village of Dzhaybalyand	10	86.5	--	1941,47 48,50,51 60,62-68 70	--	--	--	--	--	--

Table 12. Extent of Hydrometeorological Coverage

1	2	3	4	5	6	7	8	9	10	11
Alabuka, mouth of the Saychungalik River	21	129	--	1929	--	--	--	--	--	--
Alabuka, Alabukasay, 4.2 km north of Sarytal	13	208	--	1938-41 1944,52 55,57-70	--	--	--	--	--	--
Uryukty, mouth	0.3	116	1965-70	1947-70	1952-70	1951-70	--	--	--	--
Alabuka, headwater, 0.6 km above Alabuka	7.5	224	--	1940-41	--	--	1940-41	--	--	--
Sumsar-Sumarskiy, 2.6 km from the village of Sumsar	69	90	--	1941,45 50,59	--	--	--	--	--	--
Sumsar, Koklik-Kurgan kishlak	32	324	--	1933-35	--	--	--	--	--	--
Kaksarek-Koksareksay, in the center of the village of Koksarek	16	96.2	--	1941	--	--	--	--	--	--
Koksarek, city of Kara Kurgan	0.2	176	--	1927-62	--	--	--	--	--	--
Gavasay, mouth of the Beshtashata River, Verkhne-beshtashskaya	65.7	288	--	1927-62	--	--	--	--	--	--
Gavasay, mouth of the Ters River (Nizhne-Beshtashskaya)	65.3	361	1939-70	1932-70	1953-70	1936-62 1967-70	--	--	1933-70	M/CT

Table 12 (continued). Extent of Hydrometeorlogical Coverage

1	2	3	4	5	6	7	8	9	10	11
Gavasay, Burikurgan kishlak	49	503	--	1932-33	--	--	--	--	--	--
Gavasay, Kok-tash kishlak (Ukkul'dinskaya)	45	623	--	1932-33	--	--	--	--	--	--
Gavasay, Gava kishlak	41	657	1914-20 1925-70	1925-70	1945-70	1936-70	1938, 1966-69	1962-70	--	M/P
Gavasay-Mashatskiy, 3 km below the village of Yangiabab	17	--	--	1933-34 1936-62	--	--	--	--	--	--
Ters, Winter camp of Besh-Tash	1.4	30.3	--	1932-38	--	--	--	--	--	--
Beshtashata, Mouth	0.3	36.6	--	1932-38	--	--	--	--	--	--
Urtasu, Kok-tash kishlak	1.3	42.5	--	1932-33	--	--	--	--	--	--
Kassansay, Urtotokay	--	--	--	--	--	--	--	--	--	M/CT
Kassansay, Kassansay kishlak	--	--	--	--	--	--	--	--	--	M/CT
Sumsar, Sumsar kishlak	--	--	--	--	--	--	--	--	--	M/CT

Table 12 (continued). Extent of Hydrometeorological Coverage

Irrigation and Agriculture

Approximately 27% of the total land area of the USSR is agricultural, and slightly more than one-third of the agricultural land is arable. The remainder of the agricultural land is meadow, pasture, orchard, vineyard, or is idle. In 1972, of the 224 million hectares of arable land in the USSR, almost all was sown. Irrigated land at this time totaled 12 million hectares, with 43% (approximately 5 million hectares) of this located in Central Asia, where irrigation has played a major role in agriculture for centuries. As of 1970, over 800,000 hectares were irrigated in the Fergana Valley, representing more than 95% of the arable land (Lydolph, 1970). In the valley much of the water from the mountain streams is absorbed by the loose material of the alluvial fans, and the sediments deposited result in the formation of fertile soils of great agricultural value. Intensive cultivation by a large population has always been possible on the oases found at the foot of the large alluvial fans in the valley. The natural irrigation system of the alluvial fans has recently been improved with the construction of numerous irrigation canals. Because of the increase in irrigated land in the last 35 years, planting is now done on mountain slopes, along the strips bordering the canal paths, and in the glades between orchards.

The northern part of the Fergana Valley has favorable natural conditions for intensive cultivation and irrigated agriculture. The main methods of irrigation are furrow for plowed crops, and flooding along strips for cereal crops and alfalfa. The irrigated fields are tilled entirely mechanically.

Agriculture in Soviet Central Asia is largely dependent on irrigation because evaporation exceeds precipitation over most of the area. Snow and rain in the mountains to the south feed the large rivers that flow into the lowlands, depositing alluvium and providing water for extensive canal networks (CIA, 1974).

The main canal system completely encircles the basin (Figure 17), with feeder canals distributing water over much of the valley floor. Only the lowest central portion of the basin is not irrigated due to texture and brine conditions unsuitable for agriculture. Much of the water supplied to this part of the basin occurs in the form of groundwater. Almost all flow from the foothill tributaries on the margins of the Fergana Valley is diverted into canals for distribution as irrigation. Little, if any, reaches the Syr Darya.

The largest canal is the 300 km Great Fergana Canal, fed by the Naryn River and Kara Dara. It runs the length of the valley from the northeast to the southwest and forms the base for the irrigation system in the Fergana Basin (Figure 17). The Fergana Canal passes through the zone of maximum

groundwater, skirting the perimeter of the alluvial fans in the valley. A number of hydroelectrical installations, locks, sluices and other water works operate along its length (Wheeler and Footman, 1954). The function of the Canal and its subchannels is to supplement pre-existing irrication systems on the northern slopes of the Alai Range with water of the Naryn River and Kara Darya. The main canal intersects all of the irrigated fans of the rivers and streams in the southern part of the valley. The canal system begins with water from the Naryn which is transferred along the canal to the Kara Darya, dammed by Kugan-Yarskaya Dam, which raises its level by 4 m to allow water movement under gravity westward. During the period 1957 to 1959, a large irrigation dam was constructed near the apex of the Kokand alluvial fan to collect a portion of the waters of the Sokh River for the irrigation of an additional 60,000 hectares of land in the south-central section of the valley. In addition to water from the Naryn and Kara Darya, the canal system receives additional water from rivers flowing off the mountains of the Alai Range, and minor amounts from flow from the Tien Shan. Rivers of different regimes are united by the system. Rivers of predominant glacial feeding (Sokh, Isfara) with the main high water in summer, rivers of snow feeding (Kara Darya) with main high water periods in spring, and rivers of mixed feeding (Naryn, Syr Darya) with bimodal high water periods are joined in a surface water system with an almost completely adjusted regime with relatively constant flow spring and summer (Suslov, 1961). Many feeder canals distribute the water over much of the basin floor (95% of arable land) (Gregory, 1968).

The Northern and Southern Fergana Canals are the two other major irrigation systems in the valley. The South Canal is about 105 km long and irrigates the land along the foot of the mountains in the southeastern portion of the valley. In addition, many streams which flow into the valley and have built alluvial fans are used for gravity flow irrigation.

The area included in the Soviet study area is served by several irrigation systems: the Northern Fergana Canal, which irrigates 63,000 hectares; the Padshaatinskaya Canal, which irrigates 32,000 hectares, the Kassansayskaya Canal, which irrigates 24,000 hectares has a reservoir with a 165 million m^3 capacity; and the Gavasayskaya canal, serving 17,000 hectares.

The North Canal, 162 km long, provides water to the area north of and parallel to the Syr Darya. It has existed in its present form since 1960, and received water from the Uchkurganskaya storage dam on the Naryn River since 1967. The irrigation system serves a strip from 2-6 km wide along the canal. The canal is built along a hillside and traverses numerous ravines and streams. In winter the water supply is hampered by the formation of ice.

The Padshaatinskaya system is fed by the Padshaata River. Springs are an important source of water to this system. The total discharge of the springs is about 160 million m^3; the mean discharge of the river at its emergence from the mountains is 190 million m^3. There are also 100 wells with a total yield of 2-3 m^3/sec. The total length of the canals in the network is about 1100 km, of which 160 km make up the large trunk and interfarm canals. 120 km of these are concrete-lined.

The Kassanskaya irrigation system is fed by the Kassansay River, whose source is above 4000 m. Its reservoir allows seasonal regulation of flow. The trunk and interfarm canals are 176 km long, of which about 40 percent are concrete-lined.

The Gavasayskaya system gets water from the Gavasay River, which is fed by seasonal snows. Springs and wells are important to the system - springs supply about 1.5 m^3/sec; around 100 wells have a total yield of 3 m^3/sec. Of the 97 km of interfarm canals, 43 km have concrete lining.

Cultivation and processing of cotton, the valley's most valuable crop, are the chief economic activities in the Fergana Valley, and Kokand, Margelan, and Fergana are important cotton-ginning centers (Plummer, et al., 1971). This basin produces between two-thirds and three-quarters of the cotton grown in the Soviet Union (Gregory, 1968). Alfalfa is grown for livestock fodder and to reduce the inherent salinity of the soil. Wheat, barley, corn, sorghum, melons, and vegetables are also cultivated. Vegetables are grown for local urban markets. Other food grains are cultivated without irrigation.

The Fergana Valley is one of the main orchard-vineyard districts of Central Asia. Fruit crops, such as apricots, peaches, and plums, are produced, particularly around the larger cities. Fruit is also dried in local factories (Gregory, 1968). The climate of the Fergana is very favorable for the cultivation of grapes (Burikin, 1967). Rice is another major crop of the valley, although a minor food crop for the Soviet Union as a whole. Silk is produced at mulberry plantations in the valley (Figure 18).

Livestock production in the Fergana Valley includes both beef and dairy cattle breeding, and sheep breeding for mutton and wool. The distribution of meat-producing animals in the USSR follows the distribution of population, unlike the situation in the United States, where livestock tend to be concentrated in less populous states. Dairy cows in the USSR are utilized for both beef and milk, and the dairy industry is population-oriented. The Soviet livestock industry has also been labor-intensive and thus is well suited to areas of dense rural settlement (CIA, 1974), such as the Fergana Valley.

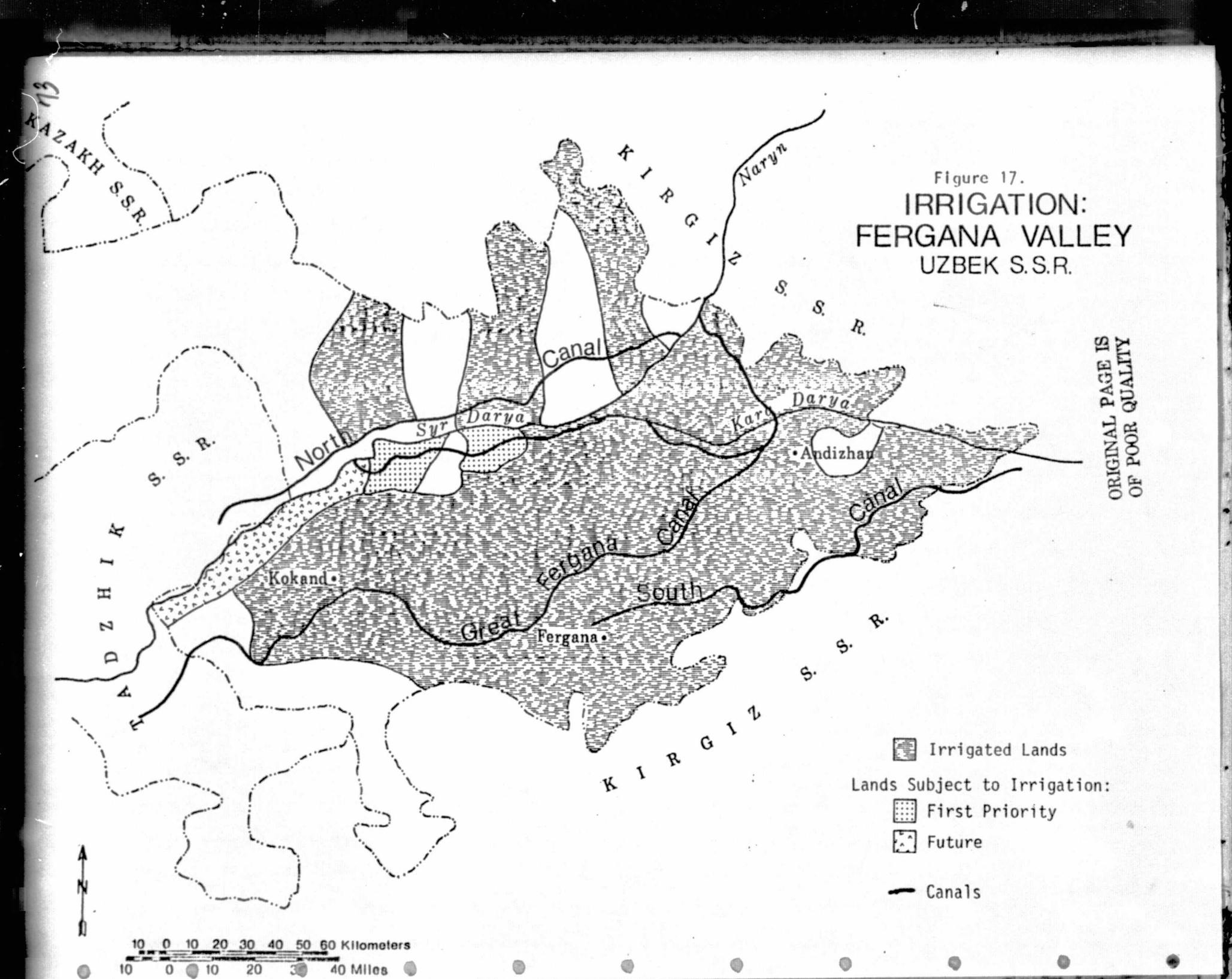

Figure 17.

IRRIGATION: FERGANA VALLEY UZBEK S.S.R.

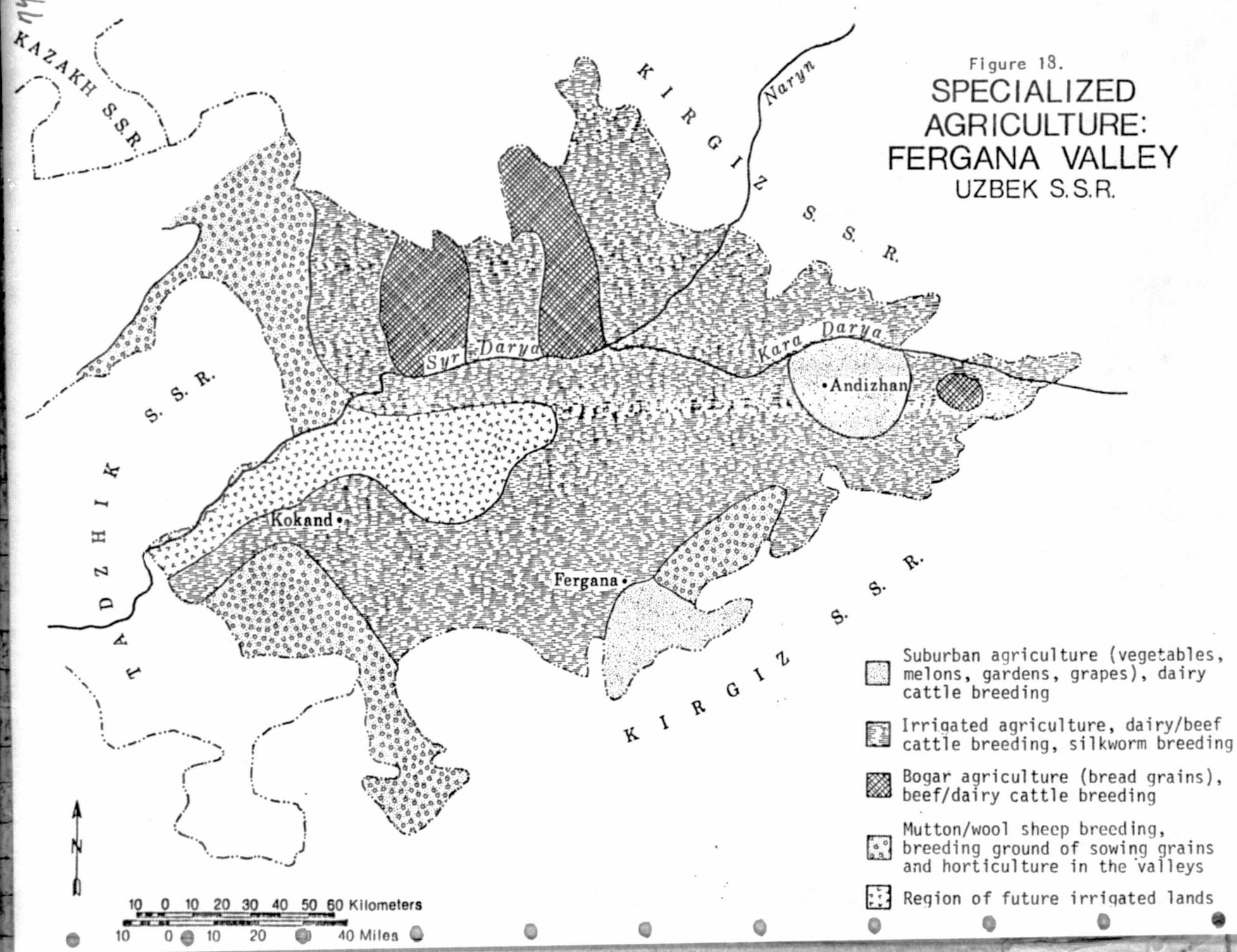

Figure 18.

SPECIALIZED AGRICULTURE: FERGANA VALLEY UZBEK S.S.R.

Industry and Manufacturing

The Fergana Valley constitutes an important economic district of the Uzbek, Tadzhik and Kirgiz SSR's. The combination of coal and iron deposits has contributed to the area's industrial development. Among the industries in the area are oil, mining, engineering, chemicals, textiles (cotton and silk), food processing (including vegetable oil and wine), and fertilizers. In spite of the Fergana's industrial productivity, Uzbekistan is not self-sufficient in steel, fertilizer, or fuel production (Gregory, 1968). Much of the industry and manufacturing in the Fergana Valley is located in a ring around the valley floor which follows the main roads and railroads that skirt the alluvial fans. Industry tends to be in greater concentration along the southern portion, and especially at the eastern end in the Andizhan region. The Kokand, Namangan, and Margelan-Fergana regions also include industrial concentrations.

Industrially, Andizhan is the most diverse city in this region, being involved with the: food; building materials; chemical; agricultural engineering; engineering; and metal-working industries. Next is Fergana, with food industry, silk, textiles, chemical industry, and oil refining. Kokand has food industry and textiles, chemical industry and engineering and metal working. Kokand lost its place as an administrative center, after the revolution, to the rising industrial center of Fergana, and consequently suffered a drop in population. However, the growth of Kokand's cotton-ginning industry and the addition of metal working and chemical fertilizer industries (phosphate and super-phosphate) have helped to revitalize the city. Namangan is involved with the food industry, textiles, and building materials (Burikin, 1967). The food industry, although found in most of the major cities, is principally concentrated at the eastern end of the valley.

The cities of Pap, in the northwest, and Shor-Su, in the southwest, are both involved with the chemical industry. Kuvasai, in the south, has a cement works and building materials industry (Burikin, 1967). Begovat was established by the Soviets as the only steel production center in Central Asia. In 1968 the annual production of steel was about 334,000 tons (Gregory, 1968). It is hoped that eventually enough steel can be produced to make the Central Asian region self-sufficient.

The Fergana Valley contains extensive deposits of oil and natural gas, principally along its southern rim. Here there are several oil and natural gas extraction centers. Several natural gas pipelines run along the southern edge of the valley (Burikin, 1967). In the Kuraman Range to the northwest of the valley floor are large depoists of low grade coal, as well as some copper, aluminum, and other minerals in lesser amounts. While the mineral deposits of the Fergana Valley are not large on a global scale, they

represent the largest concentration of extractable minerals in Central Asia, and are a major factor in the industrial productivity of the Fergana Area (Suslov, 1967). Sulphur and salt are mined near Shor-Su and salt is produced from ancient mines on the valley floor. Gold is mined near Chadak. Uranium mining began in the 1950's in the mountains north of the valley near Uygin-Say (Plummer, et al, 1971).

There are both hydro-electric and thermo-electric power stations in the Fergana Valley (Figure 19). Hydro-electric stations are found near Leninsk and Uchkurgah. Thermo-electric stations are found near Namangan, Fergana, Kuvasai and Kokand (Burikin, 1967).

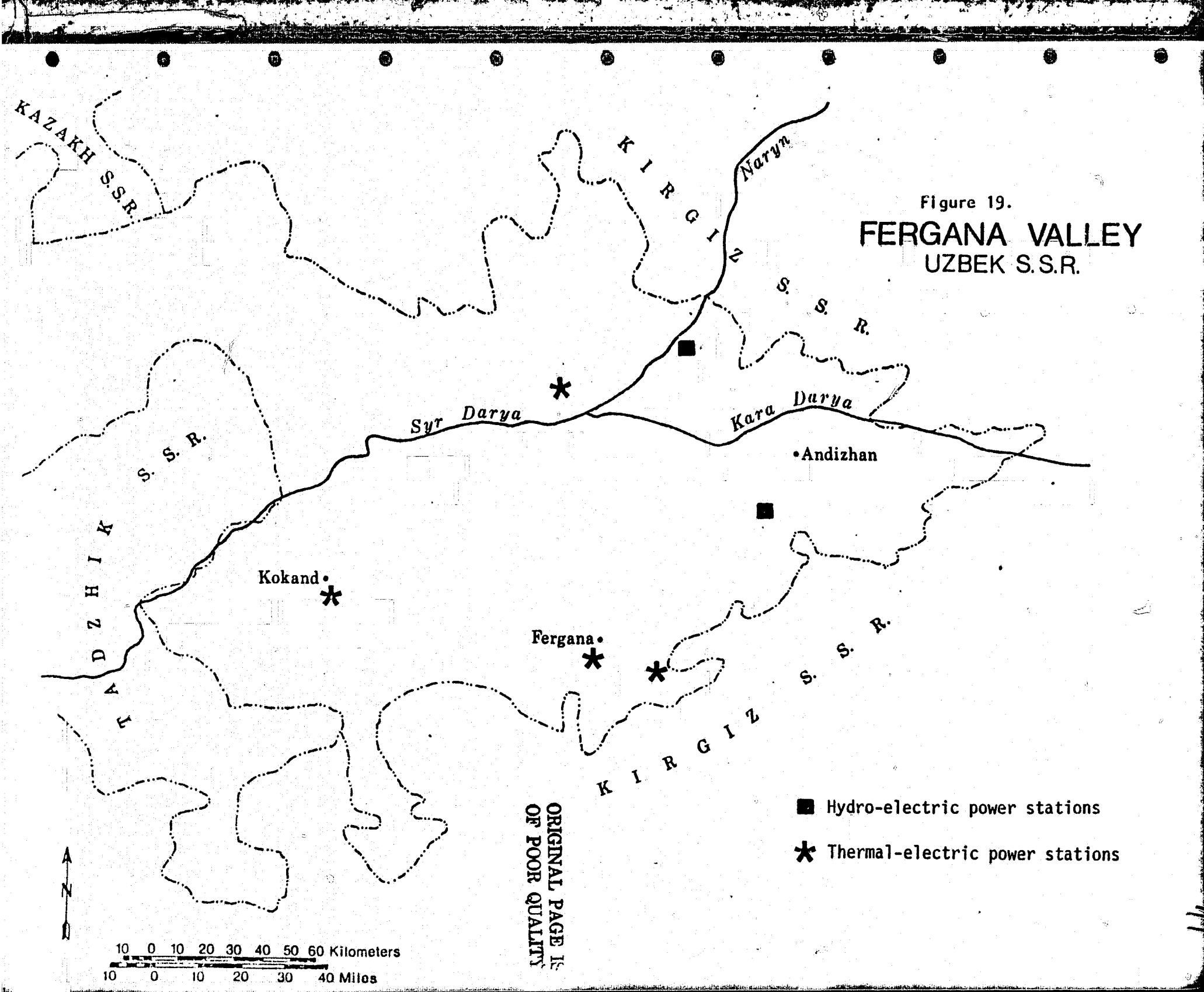

Figure 19.

FERGANA VALLEY
UZBEK S.S.R.

References for Chapter VI

Allworth, E., 1967. Central Asia: A Century of Russian Rule. Columbia University Press, New York, pp 102-112, 294-335.

Average Climatic Water Balance Data of the Continents (Part III, USSR), 1963. Thornthwaite Associates, National Science Foundation, Technical Report No 3. Centerton, New Jersey.

Baranov, A.N., 1969. Atlas of USSR, 2nd ed. Soviet Ministry, Moscow. (in Russian; transliteration: Atlas SSSR) 200 pp.

Belousov, V.V., and Gzovskii, M.V., 1958. Seismic and Recent Tectonic Map of USSR, translated by Telberg Book Co., New York. (Transliteration: Predvaditel'naia Skhema Sopostavleniia Seismichnostis neotektonikci SSSR, from Akademia Nauk SSSR, Trudy Laboratorii Vulkanologii, Vypusk 13, Moscow, 1958")

Bol'shakov, M.N., 1974. Water Resources of the Rivers of the Soviet Tien-Shan and Methods of Their Calculation. (Vodnyye resursy rek sovetskogo Tyan-Shanya i metody ikh rascheta) Ilim Press, Frunze.

Brady, N.C., 1974. The Nature and Properties of Soils, 8th ed. Macmillan, New York, 639 pp.

Burikin, A.P., (ed), 1967. Soviet Union: Uzbekistan. Misl', Moscow. (in Russian; transliteration: Sovetskii Soyuz: Uzbekistan) 320 pp.

Central Intelligence Agency, 1974. USSR Agricultural Atlas. Washington, D.C., US Gov Publication, 59 pp.

Dietz, R.S., and Holden, J.C., 1970. The Breakup of Pangaea. in Wilson, J.T., (ed), 1971. Continents Adrift. Freeman and Co., San Francisco, p 102-113.

Fetisova, N.P., (ed), 1965. Climatic Map of USSR, (in Russian; transliteration: Klimaticheskaia Karta SSSR).

Gerasimov, I.P., et al., 1976. Large-Scale Research and Engineering Programs for the Transformation of Nature in the Soviet Union and the Role of Geographers in their Implementation. Soviet Geography: Review and Translation, pp 235-245.

Gregory, J.S., 1968. Russian Land, Soviet People. Pegasus, New York, pp 807-851.

Handbook on Climate in the USSR, 1973. (Spravochnik po klimatu SSSR). Part I, No 32, Gidrometeoizdat, Leningrad.

Karpov, S.F., 1960. Dynamics of the Moisture Content of Mountain Soils, Tr. Chatkal'skoy Gorno-Melicrativnoy Opytnoy Stantsii, No 1, Tashkent.

Khadzhibayev, N.N., 1970. Natural Flows of Groundwater in Uzbekistan. (Yestestvennyye potoki gruntovykh vod Uzbekistana). Uzbek SSR Academy of Sciences, Tashkent.

Kraynova, I.P., 1975. Chemical description of the irrigation waters of the Syr-Dar'ya River Basin. Soviet Hydrology: Selected Papers, no 3. American Geograhical Society, Washington, D.C., pp 178-180.

Kritskiy, S.N., and Menkel, M.F., 1968. Water management in the USSR and problems in engineering hydrology. Soviet Hydrology: Selected Papers, no 1. American Geograhical Society, Washington, D.C., pp 1-35.

Lydolph, P.E., 1970. Geography of the USSR. John Wiley and Sons, New York, pp 217-269.

Ministry of Geology, 1964. Tectonic Map of USSR, Moscow. (in Russian; transliteration: Tektonicheskaia Karta SSSR, English legend). Sheet 14.

Ministry of Geology, 1966A. Geologic Map of USSR, Moscow. (in Russian; transliteration: Geologicheskaia Karta SSSR). Sheet 11.

Ministry of Geology, 1966B. Hydrochemical Map of USSR, Moscow. (in Russian; transliteration: Gedrokhemicheskara Karta SSSR).

Plummer, T.F., Jr., Hanna, W.G., Brunev, E.F., and Thudium, C.C., Jr., 1971. Landscape Atlas of the USSR. Dept of Earth, Space and Graphic Sciences, United States Military Academy, West Point. US Army Topograhic Command, Wasington, D.C., pp 114-115, 124-125.

Resources of Surface Waters of the USSR, 1969. (Resursy poverkhnostnykh vod SSSR). Central Asia, Syrdar'ya Basin (Srednyaya Aziya, Basseyn Syr Dar'yi), Vol 14. Gidrometeoizdat, Leningrad.

Rode, A.A., 1963. Water Regime and its Regulation (Vodnyy rezhim pochv i yego regulirovaniye), USSR Academy of Sciences Press, Moscow.

Shul'ts, V.L., 1965. Rivers of Central Asia (Reki Sredney Azii). Gidrometeoizdat, Leningrad.

Sokolov, A.A., 1976. The World Water Balance. Soviet Geography: Review and Translation, vol 3, pp 505-515.

Strahler, A.N., 1974. Physical Geography, 4th ed. Wiley, New York, plate 2.

Suslov, S.P., 1961. Physical Geography of Asiatic Russia. Freeman & Co., San Francisco, pp 436-520.

Vendrov, S.I., 1976. Problems in the Spatial Redistribution of Streamflow. Soviet Geography: Review and Translation. pp 415-420.

Volchuyev, V.B., 1976. Comparative investigation of soil units identified in some publications on the soils of the world. Soviet Soil Science, vol 8, pp 48-61.

Voznesenskiy, A.N., Gangardt, G.G., and Gerardi, I.A., 1975. Principal Trends and Prospects of the Use of Water Resources in the USSR. Soviet Geography: Review and Translation. pp 291-302.

Walter, H., and Leith, H., 1967. Klimadiagramm-Weltatlas (World Climatic Atlas), VEB Gustav Fisher Verlag, Jena, Germany. Section 1-11 (in German).

Wheeler, G.P., and Footman, D.J., (eds), 1954. Uzbekistan: Irrigation and Settlement in the Fergana Valley. Central Asian Review, vol 2, no 2, pp 134-137.

Wiebecke, C., and Tornusky, R., 1967. Welt-Forstatlas (World Forestry Atlas). Verlag Paul Parey, Hamburg and Berlin. Maps 32, 33, 34 (in German).

World Weather Records, 1959-1960, Volume 4 (Asia), 1967. US Department of Commerce, Environmental Science Services Administration, Environmental Data Service. Washington, D.C., 504 pp.

Appendix 1

Dozier, J. and Outcalt, S.I. An Approach toward Energy Balance Simulation over Rugged Terrain.

This paper has been submitted for publication to Geographical Analysis.

(submitted to Geographical Analysis)

AN APPROACH TOWARD ENERGY BALANCE SIMULATION OVER RUGGED TERRAIN

Jeff Dozier and Sam I. Outcalt*

* We are indebted to Dr. Anthony Brazel for the data used to verify model results, to Jumar G. Miya for assistance in the early stages of the programming, and to Dr. Leonard Myrup for helpful discussion and references. The contouring algorithm for the plots was modified from program CNTOUR, originally written by W. Couthard of the University of British Columbia, and which is available from the Geography Program Exchange, Michigan State University. Margie Gilson and Edwin Gustafson prepared the computer-drawn maps for publication. Computer funds for the simulations were supplied by the Research Committee of the Academic Senate, University of California, Santa Barbara, and by the National Aeronautics and Space Administration, Grant Number NSG 5155.

Jeff Dozier is assistant professor of geography at the University of California, Santa Barbara, and Sam Outcalt is associate professor of geography at The University of Michigan.

Abstract

We develop a digital computer model, based upon equilibrium temperature theory, of the magnitudes of the components of the energy balance for a mountainous topographic surface. The model includes an algorithm for calculating slope, exposure, and horizon information for every point on a digitized grid. Incoming solar and thermal radiation are then simulated for every point. At present the model is designed for clear-sky conditions, but it could be modified for cloudy skies. Air temperature and humidity variations are specified by externally defined relations, and values for albedo and soil thermal properties are specified for every point on the grid. Wind speed variation over the grid is not modeled, but is specified by an empirical function. The model simulates net radiation, soil heat flow, sensible and latent heat flow, and surface temperature at specified time intervals. Output is in the form of contour maps.

Key words: energy balance climatology, computer simulation, solar radiation, topography

INTRODUCTION

Surface energy balance models have been used to simulate accurately the surface temperature, soil heat and water flow, and snowmelt. Their operational utility over wide areas of variable terrain has been limited, however, because of the extensive data needed to drive such models. In this paper we present a method and a description of a computer program for extending energy balance simulations over rugged terrain, and illustrate a few cases of such simulations.

NOTATION

a_i Fourier cosine coefficient

a_Q beam albedo

a_q diffuse albedo

a (subscript) air

A azimuth of sun from south (negative when east of south)

b integer storage subscript for horizon angles

b_i Fourier sine coefficient

C mass heat capacity

C_p heat capacity of air at constant pressure

d dust and haze content in units of 800 particles cm^{-3}

D diabatic exchange coefficient

e vapor pressure

E azimuth of slope from south (negative when east of south)

F Fourier modulus, $= \alpha \Delta t (\Delta s)^{-2}$

g gravitational acceleration

G soil heat flow

h	grid spacing
H	sensible heat flow
$I_{\downarrow}$	incoming atmospheric (infrared) radiation
j	subscript for node
$I_{\uparrow}$	outgoing thermal radiation
J	Julian date
k	von Karman constant, = 0.4
k_a	absorption coefficient
k_s	scattering coefficient
K	thermal conductivity
L	latent heat of vaporization, = $f(T_s)$
LE	latent heat flux
m	molecular weight
M	optical air mass
p_w	precipitable water vapor
P	atmospheric pressure
q	incoming diffuse solar radiation (including backscatter)
Q	incoming beam solar radiation
Q'	incoming beam solar radiation on slope
Q_0	solar constant
r	earth's radius vector
R	gas constant
R_n	net radiation, = $Q(1-a_Q) + q(1-a_q) + I_{\downarrow} - I_{\uparrow}$
s	(subscript) surface
s	depth
S	slope from horizontal
t	time
T_a	air temperature

T_z temperature at altitude z

T_m measured temperature at altitude z_m

u wind speed

u_* friction velocity

V_f thermal radiation view factor

z altitude of surface or of temperature, wind, and humidity values

z_0 roughness length

Z solar zenith angle

Z' solar zenith angle with respect to slope

Z_H horizon angle from zenith

α thermal diffusivity, = $K/\rho C = f(T)$

δ solar declination

ε_a effective atmospheric emissivity

ε_s surface emissivity

θ potential temperature

θ_* scaling temperature

ρ density

σ Stefan-Boltzmann constant

ϕ latitude

ω hour angle of the sun from noon (negative in morning)

REVIEW OF SURFACE ENERGY BALANCE MODELS AND NUMERICAL METHODS

Broadly defined, surface energy balance models are those which simulate all of the major surface energy exchange processes, and which use the conservation of energy principle as a boundary condition. In its simplest form, over a solid surface, the principle is described by the equation:

$$R_n + H + LE + G = 0 \qquad (1)$$

In the soil, heat flow is described by the one-dimensional conduction equation:

$$\partial T/\partial t = \alpha[T,s]\ \partial^2 T/\partial s^2 \qquad (2)$$

Typically it is assumed that no diurnal heat flux occurs below a certain depth, e.g. 30 cm.

The sensible and latent heat fluxes are estimated from air temperature and humidity, surface temperature and humidity, wind speed, and roughness length, using the Businger-Dyer formulation for atmospheric temperature and wind speed profiles:

$$H = \rho_a\ C_p\ k\ u_*\ \theta_* \qquad (3)$$

$$LE = .622\ H\ L\ C_p^{-1} P^{-1}\ (e_a - e_s)\ (\theta_a - \theta_s)^{-1} \qquad (4a)$$

If $\theta_a = \theta_s$, the latent heat exchange is

$$LE = .622\ L\ k^2\ \rho_a\ u\ P^{-1}\ (e_a - e_s)\ [\ln(z/z_0)]^{-2} \qquad (4b)$$

The friction velocity u_* and the scaling temperature θ_* are given by

$$u_* = ku/[\ln(z/z_0) - \psi_1] \qquad (5)$$

$$\theta_* = (\theta_a - \theta_s)/[\ln(z/z_0) - \psi_2] \qquad (6)$$

ψ_1 and ψ_2 are the Businger-Dyer ψ-functions; their formulation and derivation are described by Paulson [38]. If only mean values of temperature, wind speed, and humidity are available, the best "calculation height" for z is given by equating the bulk adiabatic diffusivity [29] and the daily

disturbance penetration depth diffusivity [46]:

$$\frac{k^2 u}{[\ln(z/z_0)]^2} = \frac{z^2}{5.184 \times 10^5} \qquad (7)$$

This can be solved iteratively for z. Although the height estimated by this equation is typically lower than the height of the diurnal heat pulse, it provides an estimate which is consistent with the assumption that heat fluxes are constant with height in the boundary layer.

In order to evaluate the magnitudes of the various heat transfer processes, a powerful solution method based upon equilibrium temperature theory has been developed [29]. For a given set of astronomical, temporal, atmospheric, and surface boundary conditions, there is a unique surface temperature which will satisfy equations (1) through (7).

Halstead et al. [18] designed an analog computer to estimate the surface temperature and the other components. Estoque [12] adapted a similar model, driven by measured values of incoming solar radiation, air temperature at screen height, wind speed, and sub-surface soil temperature, to a digital computer. Myrup [29] simulated the urban heat island with an analog computer, illustrating the importance of soil moisture in determining the disposition of the energy balance and therefore the surface temperature. Sasamori [44] simulated atmospheric boundary layer and soil temperature profiles, plus wind velocities in the boundary layer, using a digital model driven by measured values of solar radiation, air temperature, and wind speed, at a given level. Outcalt [32] devised a digital model which simulates solar and

infrared radiation, and which may be driven by mean daily temperatures if higher-frequency observations are not available; this computer program has been revised to use the Businger-Dyer ψ-functions for turbulent heat and water vapor transfer, and adapted to a topographic surface for this paper.

To solve for the equilibrium surface temperature an initial value of T_s is chosen, and values of soil, sensible, and latent heat flow are calculated. These are used in equation (1), and the process is repeated, with iterative variations in T_s until equation (1) is satisfied within a specified margin, for example 1 Wm^{-2} or 1 mly min^{-1}. The soil temperature profile is then adjusted by equation (2), completing the time step. In the current version of the computer program we use a secant algorithm [1] to find the equilibrium surface temperature; generally it converges within three iterations. The structure of the secant algorithm is identical to that of Newton's method, except that the analytic expression for the derivative is replaced by a first-order forward difference approximation. If the left side of equation (1) is expressed generally as $f(T_s)$, then subsequent guesses for T_s are given by:

$$T_s^{n+1} = T_s^n - [f(T_s^n)(T_s^n - T_s^{n-1})][f(T_s^n) - f(T_s^{n-1})]^{-1} \quad (8)$$

There exist many schemes for numerical solution of the heat flow equation (2). The present computer program employs a fully implicit method. This has the advantage of unconditional stability, regardless of the value of the

Fourier modulus $F = \alpha \Delta t (\Delta s)^{-2}$, and the choices of Δt and Δs are governed only by the accuracy desired [42]. The soil thermal diffusivity α is a function of temperature and water content [2, 47] and thus varies with depth and time. The implicit scheme used is [42]:

$$(1+2F_j^t)(T_j^{t+1}) = T_j^t + F_j^t(T_{j+1}^{t+1}+T_{j-1}^{t+1}) \qquad (9)$$

where subscript j indicates the node and superscript t indicates the time step. Application to all nodes at one time step leads to the following tridiagonal system of simultaneous linear equations:

$$\begin{bmatrix} 1+2F_1^t & -F_1^t & 0 & 0 & 0 \\ -F_2^t & 1+2F_2^t & -F_2^t & 0 & 0 \\ 0 & -F_3^t & 1+2F_3^t & -F_3^t & 0 \\ 0 & 0 & \cdot & \cdot & \cdot \\ 0 & 0 & 0 & \cdot & \cdot \end{bmatrix} \begin{bmatrix} T_1^{t+1} \\ T_2^{t+1} \\ T_3^{t+1} \\ \cdot \\ \cdot \end{bmatrix} = \begin{bmatrix} T_1^t \\ T_2^t \\ T_3^t \\ \cdot \\ \cdot \end{bmatrix} \qquad (10)$$

Temperature at the top node is determined by equation (8) and temperature at the bottom node is held constant.

Many experiments have demonstrated that such energy balance models simulate surface temperature with reasonable accuracy, in urban [29, 33], mid-latitude [44], arctic [34, 35], and alpine [5] environments. These simulations have been verified by point surface temperature measurements and, in the case of [33], by thermal imagery.

Such models have also been coupled with simulations of soil water movement to produce combined heat and water flow models [17, 36, 43]. These have important implications for

construction in arctic areas, where the movement, freezing, and thawing of soil water may have severe consequences.

Energy balance simulation has also been applied to development of accurate snowmelt models. Outcalt et al. [37] used station weather data to simulate changes in the snow and soil thermal regimes at Barrow, Alaska. They simulated both the beginning and end of the melt period within one day of the actual times, and the depth of thaw penetration into the soil to within 5 cm. Anderson [3] compared the results of his snowmelt simulation with measurements of snow cover water equivalent at the National Oceanic and Atmospheric Administration - Agricultural Research Service cooperative snow research station near Danville, Vermont, and found that in most situations his energy balance model was superior to more conventional snowmelt models.

In cases where surface temperature is known, for example from thermal imagery from spacecraft or aircraft, energy balance models can be applied in reverse to estimate the thermal characteristics of the surface material, which can then be used to identify the surface lithology [21, 22, 39, 48]. Alternatively, if the surface lithology is also known, thermal imagery can be used to locate areas of high geothermal heat flow [9, 48]. LeSchack and Del Grande [26] have outlined a method whereby thermal sensing in two wavelength bands (e.g. 5 and 10 μm) can separate emissivity-related effects from temperature-related effects, thereby allowing determination of actual temperatures to an accuracy of 0.1 or 0.2 °K.

DATA NEEDED FOR ENERGY BALANCE SIMULATION

The application of an energy balance model to a topographic surface necessarily involves the use of a digital computer. Therefore the term "topographic surface", as used hence, refers to a digitized grid, consisting of a finite number of points. Such grids are now available at very modest cost as "Digital Terrain Tapes" from the National Cartographic Information Center, U.S. Geological Survey. In order to drive the previously described energy balance model the following parameters would have to be measured, estimated, or calculated in advance for every point on such a grid:

1. Incoming solar radiation (Q+q)
2. Albedo (a_Q and a_q)
3. Incoming longwave radiation ($I\downarrow$)
4. Air temperature (T_a)
5. Wind speed (u)
6. Surface roughness length (z_0)
7. Thermal conductivity (K) and volumetric heat capacity (ρC) of surface material (can vary with depth)
8. Air pressure (P)
9. Vapor pressure of air (e_a) and at surface (e_s)

CALCULATION OF MODEL INPUT PARAMETERS OVER A SURFACE

At this stage of model building, we do not simulate realistically all of the above parameters. The aim here is to outline the development of an energy balance model for rough terrain. In particular, we must specify, or interpolate from a set of measurements, albedo, wind speed, roughness length, and the thermal characteristics of the soil over the grid, although we calculate variations in albedo with soil wetness and illumination angle [16]. Information on albedo and perhaps roughness length are available from remote sensing, although it is necessary to simulate incoming solar radiation in order to estimate albedo. A lack of knowledge of the surface thermal characteristics is not a serious obstacle to use of the model at this time, as one of the immediate applications could be in inferring these thermal characteristics in cases where surface temperature is known from thermal imagery. Calculation of wind speeds over mountainous terrain remains a serious problem, although recent work on meso-scale wind field modelling indicates that calculations which are accurate enough to be useful might be possible [11, 13, 30].

Variation of air temperature with elevation is specified on input to the model, with a default specification of an ambient atmospheric lapse rate of $-.0065\ ^{o}K\ m^{-1}$. Air temperature T_z at altitude z can be calculated from measured temperature T_m at altitude z_m:

$$T_z = T_m - .0065(z-z_m) \qquad (11)$$

The present model does nct consider air drainage, but the computer program is so strtctured that such algorithms, if develcped, could easily be added.

Air pressure P at altitude z is derived from measured pressure P_m at altitude z_m frcm the hydrostatic equation, the equatiocn of state, and equatiocn (11):

$$dP/dz = -g\rho_a \tag{12a}$$

$$\rho_a = (Pm_a)/(RT_a) \tag{12b}$$

$$P = P_m \exp\{[(gm_a)/(.0065R)] \ln[(T_m - .0065(z-z_m))/T_m]\} \tag{12c}$$

The relative humidity of the air and of the soil surface are ccnsidered ccnstant over the grid. Specific humidities are calculated frcm empirical equations relating saturation vapor pressure to temperature [27].

Solar radiation is the major input parameter which varies widely over the grid, and an efficient method of calculating the radiation incident on every grid point is essential to the model. Many slope radiation models have been developed [14, 15, 19, 20, 24, 25, 45, 49] and we present the pertinent equations from these only briefly. They are fully outlined in the original sources.

Initially the beam and diffuse components of solar radiatiocn on a horizcntal plane at the earth's surface must be estimated cr measured. Under clear skies, these can be calculated frcm the dust and water vapor content of the atmosphere and the solar gecmetry. The beam radiation is:

$$Q = (Q_0/r^2)\ \cos Z\ \exp[k_a + k_s] \qquad (13)$$

Brooks [6] has given approximations for the absorption and scattering coefficients:

$$k_a = -.089\,(PM/1013)^{.75} - .174\,(p_w M/20)^{.6} \qquad (14)$$

$$k_s = -.083\,(Md)^{.9} \qquad (15)$$

Typical values for the dust and haze content d range from 0.2, for very clear atmospheres, to as high as 3.0 [15]. At present work is underway to define wavelength-dependent absorption and scattering coefficients from measurements of global radiation at different solar zenith angles. The optical air mass M is determined by Kasten's formula [23]:

$$M = 1/[\cos Z + .15(90 - Z + 3.885)^{-1.253}] \qquad (16)$$

where Z is the solar zenith angle in degrees. The beam radiation Q' incident upon an unshaded slope is:

$$Q' = (Q_0/r^2)\ \cos Z'\ \exp[k_a + k_s] \qquad (17)$$

In calculating the radiation on an actual slope a test must be made to determine whether the sun is shaded by a local horizon. If so, Q' = 0. Z, the solar zenith angle, and Z', the solar angle measured from normal to the slope, are given by:

$$\cos Z = \sin\phi\ \sin\delta + \cos\phi\ \cos\delta\ \cos\omega \qquad (18)$$

$$\cos Z' = \cos S\ \cos Z + \sin S\ \sin Z\ \cos(A - E) \qquad (19)$$

The azimuth of the sun from south, negative when east of south, is given by:

$$\cos A = (\sin\Phi \cos Z - \sin\delta)/(\cos\Phi \sin Z) \qquad (20)$$

Since the cosine function is even, this equation gives two possible angles for the azimuth of the sun, A or -A. If ω is negative, then the negative value for A is chosen; otherwise the positive value for A is used. A four-term Fourier series gives the solar declination in radians and the radius vector to about four significant figures:

$$\delta, r = \sum_{i=0}^{3} a_i \cos[2\pi(J-1)i/366] + b_i \sin[2\pi(J-1)i/366] \qquad (21)$$

Values for the cosine and sine coefficients for each series are in Table 1.

The diffuse radiation slope factor is $\cos^2(S/2)$ [24], and the diffuse radiation q is the sum of the downscattered radiation and backscattered radiation:

$$q = 0.5[1-\exp(k_s)][Q_0/r^2]\{\cos^2(S/2) + 0.5a_q[1-\exp(k_s)] + a_Q Q\} \qquad (22)$$

In equation (22) a_Q and a_q refer to the beam and diffuse albedo on the surrounding region. In cases where the solar zenith angle $Z < 50°$, $a_Q = a_q$, but at larger angles, the beam albedo must be corrected for glint effects [16].

Calculations for horizon angles, slope, and exposure must be made at each grid point. The method presented here

C-2

is different from that of Williams et al. [49]. If more than one simulation for the same topographic surface is made, it is more efficient, because the complete horizon and slope calculations are stored on a disk or tape file, and need not be recomputed for different sun paths. Slopes can be calculated from:

$$\tan S = [(\partial z/\partial x)^2 + (\partial z/\partial y)^2]^{1/2} \qquad (23)$$

The azimuth of the slope from south is given by:

$$\tan E = (\partial z/\partial x)/(\partial z/\partial y) \qquad (24)$$

This function is defined even if the denominator is zero, and if the signs of both the numerator and denominator are known, the function is defined over the range $-\pi$ to π. The origin for the x- and y-coordinates is assumed to be in the southwest corner of the grid, but the equations and the program can be easily modified for other orientations.

The partial derivatives $\partial z/\partial x$ and $\partial z/\partial y$ must be evaluated by numerical means, and it is necessary to choose a method which can be adjusted when the point in question is near a boundary of the grid. We use the following group of methods: (i) if the point is on the boundary, we use a second-order forward difference approximation; (ii) if the point is in the row or column next to the boundary, we use a second-order central difference approximation; (iii) if the point is in the third row or column from the boundary, we use a fourth-order central difference approximation; (iv) if the point is greater than three rows or columns from the

boundary, we use a sixth-order central difference approximation. Computational formulas for each of these approximations can be found in [4].

A set of horizon angles $\{Z_H\}$ is generated by calculating the tangent of the angle from the specified point to every other point in the grid whose elevation is greater. For example the calculation from point [m,n] to [i,j] is:

$$\tan S[mn,ij] = (z_{ij}-z_{mn})\ \{h^2[(i-m)^2+(j-n)^2]\}^{-1/2} \qquad (25)$$

Within each of a set of azimuthal increments, for example 3.75, 5, or 10 degrees, the program stores the maximum value of the tangent. If b is the sector number of size w, then

$$b = \text{int}\{\tan^{-1}[(j-n)/(i-m)]/w\} \qquad (26)$$

The maximum value of tanS[mn,b] is selected for each b. From these the horizon angles, from zenith, are calculated:

$$Z_{Hb} = \text{ctn}^{-1}\{\tan S[ij,b]\} \qquad (27)$$

This sequence results in very efficient computer code. Comparison of tangents of angles, delaying calculation of the actual angles until the maximum tangents are selected, minimizes the number of trigonometric functions that are computed.

Incoming long-wave radiation from clear skies is calculated by Brutsaert's method [7]:

$$I\downarrow = \varepsilon_a \sigma T_a^4 \qquad (28)$$

where the effective atmospheric emissivity is:

$$\varepsilon_a = 1.24(e_a/T_a)^{1/7} \tag{29}$$

A recent test of Brutsaert's method, using data from southern France, indicated that its accuracy compared favorably with that of other methods [28]. For calculation of the net long-wave radiation, the thermal radiation view factor V_f is given by Reifsnyder and Lull [41]:

$$V_f = \cos^2(\langle Z_H \rangle) \tag{30}$$

where $\langle Z_H \rangle$ is the mean horizon angle, from zenith. The diffuse radiation slope factor is $\cos^2(S/2)$, and the net long-wave radiation at the site is then:

$$I = I\downarrow - I\uparrow = \cos^2(S/2)\ [(1-V_f)\ I\downarrow + (V_f-1)\ \varepsilon_s \sigma T_s^4] \tag{31}$$

RESULTS OF SIMULATION

The computer program resulting from equations (1) through (31) was tested on a digitized topographic grid from the Chitistone Pass area (latitude 61.6°N) in the Wrangell Mountains, Alaska, and located on the McCarthy C-3 1:63360 quadrangle. We selected the area because a limited set of test data was available [5]. The area is about 3 km by 3 km and ranges in elevation from about 1500 to 2100 m. The nearby surrounding terrain includes elevations up to 2800 m, and this terrain combined with the low sun angles produces important horizon effects. From the NCIC Digital Terrain Tapes, we extracted a grid at 63.5 m spacing which spanned an area of about 11 x 10 km. From these terrain data, we calculated the horizon vectors for the study area. The output presented in this paper is in the form of contour maps; the program will also draw perspective plots if desired. Figure 1 is a topographic map of the study area and the surrounding terrain.

For the simulation we used the input parameter values listed in Table 2 below. The initial soil temperature was assumed to be equal to the air temperature to a depth of 1 m, and 24 hrs of temperature evolution were simulated to establish realistic initial conditions. Values for porosity, thermal conductivity, and roughness length were taken from field measurements [5] and estimated over the rest of the study area from a map of landforms [10]. Figure 2 illustrates the terrain of the study area itself and the distribution of

101

surface materials. Thermal properties for the different surface materials are given in Table 3.

Figure 3 illustrates the distribution of incoming solar radiation at 0600, 1000, 1400, and 1800 hours. The effects of slope, exposure, and horizon can be seen in these maps. For example, the point labelled A in figures 2 and 3 is on an east-facing slope and receives maximal radiation at 0600 and 1000. At 1400 and 1800 the intensity of the solar radiation at A is small. Point B is located on a north-facing slope, and radiation values are low at all times, especially at 1000 and 1400.

Figure 4 illustrates the distribution of net all-wave radiation at 4-hr intervals from 0200 to 2200. Uniform surface emissivity is assumed. The major source of variation is incoming solar radiation, as demonstrated by the maps for times when the sun is not up, 0200 and 2200.

Figure 5 shows integrated values of incoming solar radiation and net all-wave radiation over 24 hrs. The sharpest gradients occur in conjunction with north-facing slopes, as at point C (which is also indicated on figure 2).

Figure 6 illustrates surface temperature at 4-hr intervals. The effects of different surface materials are obvious on the 0200 and 2200 maps, where the sharp temperature gradients coincide with the surface material transitions. During the day, the temperature differences due to topographic effects overwhelm those due to the thermal properties of the soil.

DISCUSSION OF RESULTS

Tables 4 and 5 present a comparison of field surface temperature measurements with model results for five sites, whose locations are indicated on figure 2. The temperature data are from [5], wherein an earlier version of the climate simulator was shown to give realistic results, given the availability of site-specific input data. Two abstractions of the data are compared with the model.

One is amplitude and phase comparison between observed and simulated values (table 4). Although the model underestimates the amplitudes, it does rank them in the correct order. The phases (time of maximum temperature) are also correctly ranked. The other comparison used is the difference between the 2:30 a.m. and 1:30 p.m. temperatures (table 5), which correspond to the overpass times of the Heat Capacity Mapping Mission Satellite (HCMM). Here the observed differences are less than the diurnal amplitudes, because of slope and exposure effects. The model results correspond reasonably well to the data.

For these limited verification data, the model results are encouraging. However, the observed and simulated temperatures do not match exactly, and these discrepancies are probably related to four effects. The first is an inadequate evaluation of some of the surface parameters, most notably roughness length and thermal diffusivity, both of which are difficult to measure.

The second is model oversimplification. The solar radiation attenuation calculations in the present model are non-spectral and do not include specular reflection from adjacent terrain. Furthermore mean daily values for air temperature, relative humidity, and wind speed are used. An altitude correction is applied to the air temperatures, but otherwise spatial uniformity is assumed, and advection is not considered. Therefore the model results are somewhat overgeneralized.

Thirdly, the measured surface temperatures may be in error. The method that was used was to place a thermistor at the surface but shield it from radiation. Under these circumstances, the direction of the error would be toward larger amplitudes.

The fourth is the resolution of the Digital Terrain Tapes. These tapes were made from the 1:250,000 topographic maps and tend to give a smoothed picture of the terrain, thereby reducing thermal contrast.

Because of these limitations, a full test of the model will have to await the availability of thermal imagery of mountainous terrain. We suggest, however, that the results are sufficiently encouraging to indicated that for at least some applications, the model is adequate.

The model has some immediate uses. One critical parameter which would need to be measured over an area before the surface equilibrium temperature could be accurately

simulated is the surface albedo. However, the albedc cannot be reliably measured remctely unless the incoming solar radiation at all points on the surface can be accurately simulated. Otterman and Fraser [31] have successfully measured albedc from LANDSAT over horizontal terrain, but, for rough terrain, maps of solar radiation, like those of figure 3, would be a necessary prerequisite to remote measurement of albedc.

In the present applicatcn, the wind speed was relatively uniform over the study area. If the surface temperature is to be accurately simulated over a larger elevation range in mountainous terrain, the air flow and drainage will also have to be modeled. Alternatively, in cases where thermal data are available from aircraft or spacecraft, the mcdel could be revised to solve for wind speed.

The present model is designed for either bare soils or low, grassy vegetatcn. Tc apply it to an area of brush, forest, or cropland, where a definite canopy exists, the radiation attenuation by the canopy would have to be considered [40] and the convective processes in the canopy would have to be modelled [8].

During periods of cloudy weather, the simulatcn of incoming short- and long-wave radiation becomes more difficult. For scme applicatcns of the model, for example geological prospecting from thermal imagery, overcoming this problem is not necessary, because imagery would only be

available on clear days. However, if the model were used to aid in the simulation of some surface process over a longer time period, the energy budget would also have to be calculated on cloudy days. The need for supporting measurements of solar radiation would increase on cloudy days. In particular, both the beam and diffuse components would need to be measured, so that proper compensation of slope and exposure effects could be made. If, however, accurate measurements were available, the absorption and scattering coefficients could be determined from the measurements instead of from equations (14) and (15). Application of the model during partially cloudy weather would require careful analysis of the time distribution of the cloud cover.

Incoming long-wave radiation is more difficult to determine, and for some applications of the model an accurate estimation would be quite important. For example, melting snow typically has a relatively high albedo in the short-wave range, thereby reducing the importance of solar radiation and consequently increasing the importance of thermal radiation as an energy source. It is probable that cloud temperature estimates from satellite measurements could be used to estimate an effective atmospheric emissivity, and this appears to be an area for useful research in the future.

REFERENCES

1. Acton, F.S. Numerical Methods that Work. New York: Harper and Row, 1970.

2. Anderson, D.M., A.R. Tice, and H.L. McKim. "The Unfrozen Water and Apparent Specific Heat Capacity of Frozen Soils." North American Contributions, 2nd International Conference on Permafrost. Washington: National Academy of Sciences, 1973, pp. 289-295.

3. Anderson, E.A. "A Point Energy and Mass Balance Model of a Snow Cover." National Oceanic and Atmospheric Administration, Technical Report NWS 19, 1976.

4. Bickley, W.G. "Formulae for Numerical Differentiation." Mathematical Gazette, 25 (1941), 19-27.

5. Brazel, A.J., and S.I. Outcalt. "The Observation and Simulation of Diurnal Surface Thermal Contrast in an Alaskan Alpine Pass." Archiv für Meteorologie, Geophysik und Bioklimatologie, ser. B, 21 (1973), 157-174.

6. Brooks, F.A. An Introduction to Physical Micrometeorology. Davis: University of California, 1959.

7. Brutsaert, W. "On a Derivable Formula for Long-Wave Radiation from Clear Skies." Water Resources Research, 11 (1975), 742-745.

8. Deardorff, J.W. "Efficient Prediction of Ground Surface Temperature and Moisture, with Inclusion of a Layer of Vegetation." Journal of Geophysical Research, 83 (1978), 1889-1903.

9. Del Grande, N.K. "An Advanced Airborne Infrared Method for Evaluating Geothermal Resources." Proceedings, 2nd U.N. Symposium on the Development and Use of Geothermal Resources. San Francisco, 1975.

10. Detwyler, T.R., and A.L. Bedente. "Map of Landforms of the Chitistone Pass and Skolai Pass Area, Alaska." in Icefield Ranges Research Project, Scientific Results, vol. 4, edited by V.C. Bushnell and M.G. Marcus. New York: American Geographical Society, 1974, p. 385.

11. Djolov, G.D. "Modeling of Interdependent Diurnal Variation of Meteorological Elements in the Boundary Layer." Khidrologiya i Meteorologiya, 26 (1974), 3-20.

12. Estoque, M.A. "A Numerical Model of the Atmospheric Boundary Layer." Journal of Geophysical Research, 68 (1963), 1103-1113.

13. Fosberg, M.A., W.E. Marlatt, and L. Krupnak. "Estimating Airflow Patterns over Complex Terrain." U.S. Forest Service, U.S. Department of Agriculture, Research Paper RM-162, 1976.

14. Garnier, B.J., and A. Chmura. "A Method of Calculating the Direct Shortwave Radiation Income of Slopes." Journal of Applied Meteorology, 7 (1968), 796-800.

15. Gates, D.M. Energy Exchange in the Biosphere. New York: Harper and Row, 1962.

16. Geiger, R. The Climate Near the Ground, 4th ed., trans. Scripta Technica, Inc. Cambridge: Harvard University Press, 1966.

17. Guymon, G.L., and J.N. Luthin. "A Coupled Heat and Moisture Transport Model for Arctic Soils." Water Resources Research, 10 (1974), 995-1003.

18. Halstead, M.H., R.L. Hickman, W. Covey, and J.D. Merryman. "A Preliminary Report on the Design of a Computer for Micrometeorology." Journal of Meteorology, 14 (1957), 308-325.

19. Hay, J.E. "Computation Model for Radiative Fluxes." Journal of Hydrology (New Zealand), 10 (1971), 36-48.

20. Joseph, J.H. "On the Calculation of Solar Radiation Fluxes in the Troposphere." Solar Energy, 13 (1971), 251-261.

21. Kahle, A.E., A.B. Gillespie, A.F.H. Goetz, and J.D. Addington. "Thermal Inertia Mapping." Proceedings, 10th International Symposium on Remote Sensing, Ann Arbor, 2 (1975), 985-990.

22. Kahle, A.B. "Derivation of a Thermal Inertia Image from Remotely Sensed Data." Proceedings, Caltech/JPL Conference on Image Processing Technology: Data Sources and Software for Commercial and Scientific Applications. Pasadena: Jet Propulsion Laboratory, JPL SP 43-30, 1976, ch. 11, 1-8.

23. Kasten, F. "A New Table and Approximation Formula for the Relative Optical Air Mass." Archiv für Meteorologie, Geophysik und Bioklimatologie, ser. B, 14 (1966), 206-223.

24. Kondratyev, K.Ya. Radiation in the Atmosphere. New York: Academic Press, 1969.

25. Lee, R. "Theory of the 'Equivalent Slope'." Monthly Weather Review, 90 (1962), 165-166.

26. LeSchack, L.A., and N.K. Del Grande. "A Dual-Wavelength Thermal Infrared Scanner as a Potential Airborne Geophysical Exploration Tool." Geophysics, 41 (1976), 1318-1336.

27. List, R.J., editor. Smithsonian Meteorological Tables, 6th ed. Washington: Smithsonian Institution Press, 1966.

28. Mermier, M., and B. Seguin. "Comment on 'On a Derivable Formula for Long-Wave Radiation from Clear Skies' by W. Brutsaert." Water Resources Research, 12 (1976), 1327-1328.

29. Myrup, L.O. "A Numerical Model of the Urban Heat Island." Journal of Applied Meteorology, 8 (1969), 908-918.

30. Nickerson, E.C., and E.L. Magaziner. "A 3-Dimensional Simulation of Winds and Non-Precipitating Orographic Clouds over Hawaii." National Oceanic and Atmospheric Administration, Technical Report ERL 377-APCI 39, 1976.

31. Otterman, J., and R.S. Fraser. "Earth-Atmosphere System and Surface Reflectivities in Arid Regions from LANDSAT MSS Data." Remote Sensing of Environment, 5 (1976), 247-266.

32. Outcalt, S.I. "The Development and Application of a Simple Digital Surface Climate Simulator." Journal of Applied Meteorology, 11 (1972), 629-636.

33. Outcalt, S.I. "A Reconnaissance Experiment in Mapping and Modeling the Effect of Land Use on the Urban Thermal Regime." Archiv für Meteorologie, Geophysik und Bioklimatologie, ser. B, 20 (1972), 253-260.

34. Outcalt, S.I. "The Simulation and Implications of Thermal Plumes Produced by Arctic Construction in Smooth Terrain." Archiv für Meteorologie, Geophysik und Bioklimatologie, ser. B, 20 (1972), 261-267.

35. Outcalt, S.I. "The Simulation of Diurnal Surface Thermal Contrast in Sea Ice and Tundra Terrain." Archiv für Meteorologie, Geophysik und Bioklimatologie, ser. B, 21 (1973), 147-156.

36. Outcalt, S.I., and J.H. Carlson. "A Coupled Soil Thermal Regime Surface Energy Budget Simulator." Proceedings, Conference on Soil-Water Problems in Cold Regions, Calgary, Alberta. Washington: American Geophysical Union, 1975, pp. 1-32.

37. Outcalt, S.I., C. Goodwin, G. Weller, and J. Brown. "Computer Simulation of the Snowmelt and Soil Thermal Regime at Barrow, Alaska." Water Resources Research, 11 (1975), 709-715.

38. Paulson, C.A. "The Mathematical Representation of Wind Speed and Temperature Profiles in the Unstable Atmospheric Surface Layer." Journal of Applied Meteorology, 9 (1970), 857-861.

39. Rohn, H.A., T.W. Offield, and K. Watson. "Thermal Inertia Mapping from Satellite--Discrimination of Geologic Units in Oman." Journal of Research, U.S. Geological Survey, 2 (1974), 147-158.

40. Price, A.G., and T. Dunne. "Energy Balance Computations of Snowmelt in a Subarctic Area." Water Resources Research, 12(1976), 686-694.

41. Reifsnyder, W.E., and H.W. Lull. "Radiant Energy in Relation to Forests." U.S. Forest Service, U.S. Department of Agriculture, Technical Bulletin 1344, 1965.

42. Richtmyer, R.D., and K.W. Morton. Difference Methods for Initial-Value Problems, 2nd ed. New York: Wiley Interscience, 1967.

43. Rosema, A. "A Mathematical Model for the Simulation of the Thermal Behaviour of Bare Soils, Based on Heat and Moisture Transfer." Delft: NIWARS, Pub. 11, 1975.

44. Sasamori, T. "A Numerical Study of Atmospheric and Soil Boundary Layers." Journal of the Atmospheric Sciences, 27 (1970), 1122-1137.

45. Sellers, W.D. Physical Climatology. Chicago: University of Chicago Press, 1965.

46. Terzaghi, K. "Permafrost." Journal of the Boston Society of Civil Engineers, 39 (1952), 319-368.

47. de Vries, D.A. "Thermal Properties of Soils." in Physics of Plant Environment, 2nd ed., edited by W.R. van Wijk. Amsterdam: North-Holland, 1966, pp. 210-235.

48. Watson, K. "Geologic Applications of Thermal Infrared Images." IEEE Proceedings, 63 (1975), 128-137.

49. Williams, L.D., E.G. Barry, and J.T. Andrews. "Application of Computed Global Radiation for Areas of High Relief." Journal of Applied Meteorology, 11 (1972), 526-533.

Table 1

Fourier Coefficients for Solar Declination and Radius Vector

Solar Declination (radians)

i	a_i (cosine coefficient)	b_i (sine coefficient)
0	$.5796702596 \times 10^{-2}$	0.0
1	$-.3999070840$	$.7359755022 \times 10^{-1}$
2	$-.6068166326 \times 10^{-2}$	$.7560534210 \times 10^{-3}$
3	$-.2363085071 \times 10^{-2}$	$.1389717739 \times 10^{-2}$

Radius Vector

i	a_i (cosine coefficient)	b_i (sine coefficient)
0	$.1000108431 \times 10^{1}$	0.0
1	$-.1673661579 \times 10^{-1}$	$-.4951856474 \times 10^{-3}$
2	$-.1203091198 \times 10^{-3}$	$-.1790695747 \times 10^{-4}$
3	$.3517325527 \times 10^{-5}$	$-.1608389648 \times 10^{-5}$

Table 2

Input Parameter Values for Simulation

Date	August 4
Air Pressure	835.0 mb (at 1790 m)
Dust content of atmosphere	0.2 (i.e. 160 part cm^{-3})
Precipitable water	20 mm
Air temperature	7.4°C
Air relative humidity	0.81
Dry albedo	0.20 to 0.33
Wet albedo	0.15 to 0.24
Soil surface relative humidity	0.30 to 0.70
Wind velocity	2 m sec^{-1}
Roughness length	.02 to .10 m
Soil porosity	.08 to .48
Soil thermal conductivity	.87 to 4.6 W m^{-1} $°K^{-1}$

Table 3

Thermal Properties of Surface Materials (see figure 2)

	thermal conductivity W m^{-1} $°K^{-1}$	porosity	soil water fraction	z_0 (m)	albedo
Residual debris					
0 to .1 m	.87	.28	1.0	.02	.2 to .3
.1 to .2 m	4.5	.48	1.0		
.2 to 9 m	.71	.10	1.0		
Areas of mass movement					
0 to .3 m	.92	.30	.7	.05	.24 to .33
.3 to 9 m	1.4	.08	.7		
Bedrock slopes with surface debris					
0 to .3 m	2.7	.30	.3	.02	.15 to .20
.3 to 9 m	1.4	.30	.3		
Moraine					
0 to >1 m	4.6	.40	.5	.10	.15 to .20

117

Table 4

Comparison of Temperature Amplitude and Phase

	Amplitude		Phase	
Site	Observed	Simulated	Observed	Simulated
1	17.1	14.8	1130	1215
2	16.5	14.8	1210	1230
3	18.3	16.6	0930	1100
4	31.5	20.1	0930	1115
5	20.5	18.1	1600	1500

Table 5

Comparison of 2:30 a.m. and 1:30 p.m. Temperatures

	2:30 a.m.		1:30 p.m.	
Site	Observed	Simulated	Observed	Simulated
1	3.5	5.2	16.4	19.4
2	4.7	5.2	18.3	19.5
3	5.0	5.2	20.8	21.4
4	2.8	4.9	17.0	18.8
5	5.0	3.1	19.0	16.9

	Difference	
Site	Observed	Simulated
1	12.9	14.2
2	13.6	14.3
3	15.8	16.2
4	14.2	13.9
5	14.0	13.8

Captions for Figures

1. Contour map of test area and surrounding terrain. Contour interval is 100 m.

2. Enlarged contour map of test area at contour interval of 25 m, and map of surface materials. Numbered points identify locations where surface temperature data are available. Points marked by letter are referenced in text and subsequent figures.

3. Incoming solar radiation on August 4, from 0600 to 1800 (solar time). Contour interval is 50 W m^{-2}.

4. Net all-wave radiation on August 4, from 0200 to 2200 hrs. Contour interval is 50 W m^{-2}, with supplementary contours at 25 W m^{-2}.

5. Net daily solar radiation (left) and net all-wave radiation (right) on August 4. Contour interval is 2 MJ m^{-2}.

6. Surface equilibrium temperature (°C) from 0200 to 2200 hrs on August 4. Contour interval is 2°.

FIGURE 1

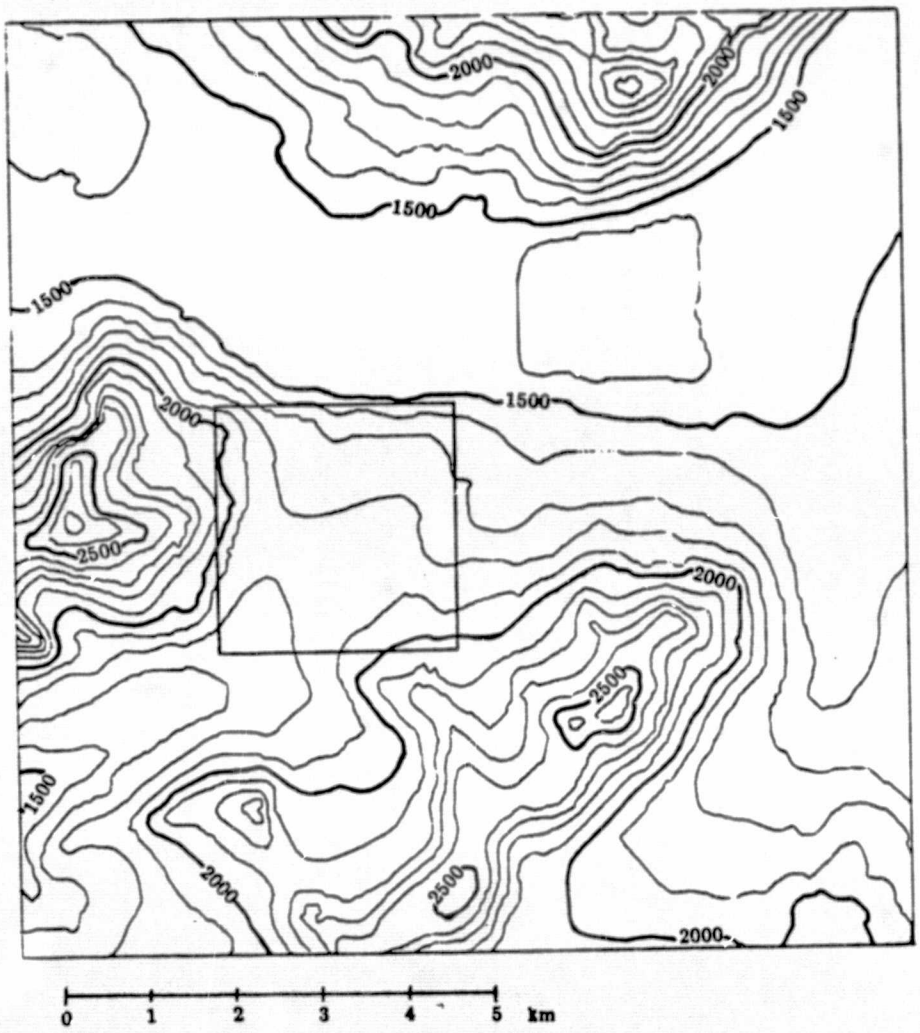
2000
2000
1500
1500
1500
1500
2000
2500
2000
2500
1500
2000
2500
2000
0 1 2 3 4 5 km

FIGURE 2

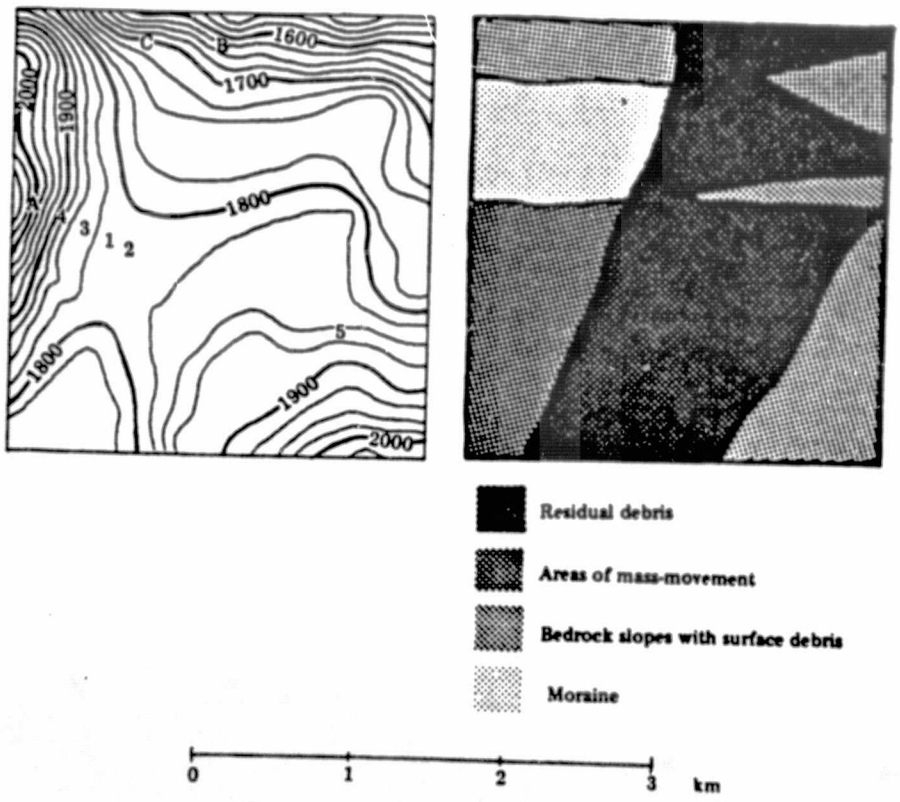

(scale for all subsequent figures)

FIGURE 5

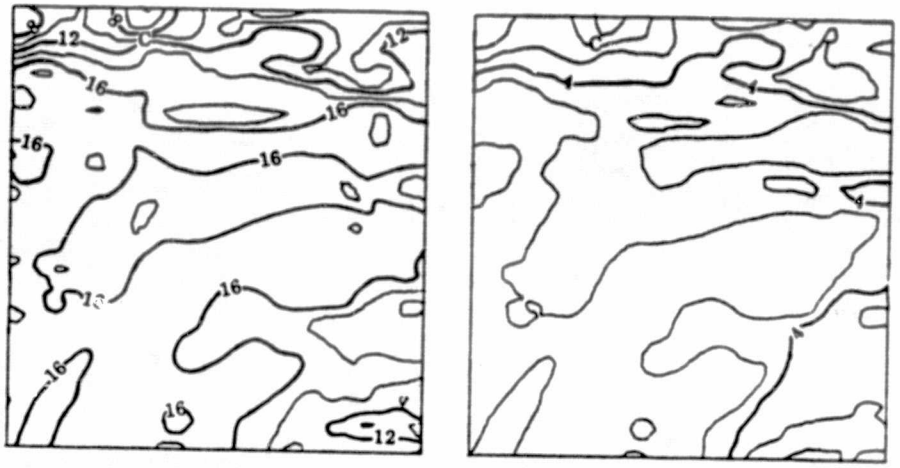

ORIGINAL PAGE IS
OF POOR QUALITY

FIGURE 3

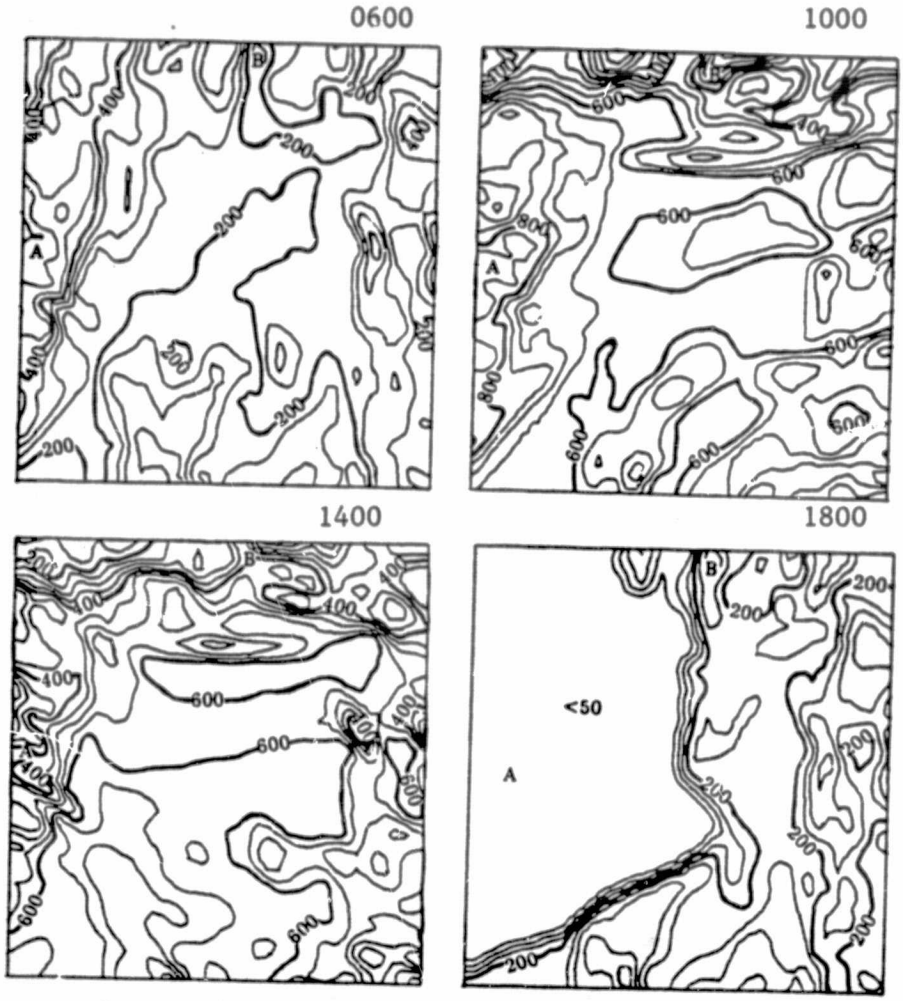

FIGURE 4

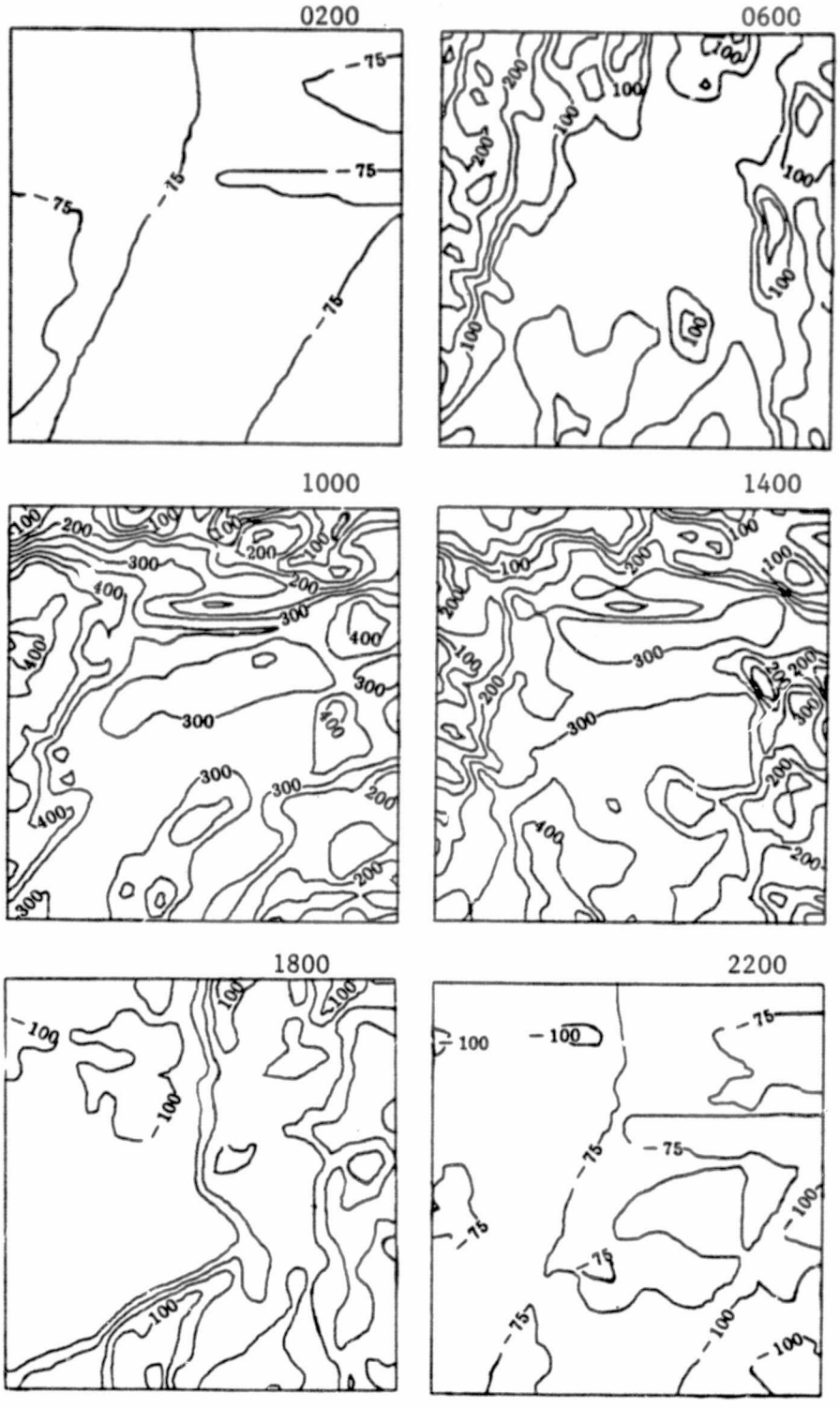

FIGURE 6